Orbital CO$_2$ reconstruction using boron isotopes during the late Pleistocene, an assessment of accuracy.

Elwyn de la Vega[ab], Thomas B. Chalk[ac], Mathis P. Hain[d], Megan R. Wilding[a], Daniel Casey[a], Robin Gledhill[a], Chongguang Luo[ae], Paul A. Wilson[a], Gavin L. Foster[a].

[a]School of Ocean and Earth Science, National Oceanography Centre Southampton, University of Southampton, Waterfront campus, Southampton SO14 3ZH, UK.
[b]University of Galway, Ollscoil na Gaillimhe, School of Geography, Archaeology & Irish Studies, University Road, Galway, H91 TK33, Ireland.
[c]Aix Marseille Université, CNRS, IRD, INRAE, CEREGE, Aix-en-Provence, France [d]Earth and Planetary Sciences, University of California, Santa Cruz, CA, USA.
[e]State Key Laboratory of Ore Deposit Geochemistry, Institute of Geochemistry, Chinese Academy of Sciences, Guiyang 550081, P.R. China.

Correspondence to Elwyn de la Vega: elwyn.delavega@universityofgalway.ie

Abstract.

Boron isotopes in planktonic foraminifera are a widely used proxy to determine ancient surface seawater pH, and by extension atmospheric CO$_2$ concentration and climate forcing on geological time scales. Yet, to reconstruct absolute values for pH and CO$_2$, we require a $\delta^{11}B_{\text{foram-borate}}$ to pH calibration and independent determinations of ocean temperature, salinity, a second carbonate parameter, and the boron isotope composition of seawater. Although $\delta^{11}B$-derived records of atmospheric CO$_2$ have been shown to perform well against ice core-based CO$_2$ reconstructions, these tests have been performed at only a few locations and with limited temporal resolution. Here we present two highly resolved CO$_2$ records for the late Pleistocene from ODP Sites 999 and 871. Our $\delta^{11}B$-derived CO$_2$ record shows a very good agreement with the ice core CO$_2$ record with an average offset of 13±46 (2σ), and a RMSE of 26 ppm, with minor short-lived overestimations of CO$_2$ (of up to ~50 ppm) occurring during some glacial onsets. We explore potential drivers of this disagreement and conclude that partial dissolution of foraminifera has a minimal effect on the CO$_2$ offset. We also observe that the general agreement between $\delta^{11}B$-derived and ice core CO$_2$ is improved by optimising the $\delta^{11}B_{\text{foram-borate}}$ calibration. Despite these minor issues a strong linear relationship between relative change in climate forcing from CO$_2$ (from ice core data) and pH change (from $\delta^{11}B$) exists over the late Pleistocene, confirming that pH change is a robust proxy of climate forcing over relatively short (<1 million year) intervals. Overall, these findings demonstrate that the boron isotope proxy is a reliable indicator of CO$_2$ beyond the reach of the ice cores and can help improve determinations of climate sensitivity for ancient time intervals.

1- Introduction.

The boron isotope composition of ancient planktonic foraminifera shells is widely used to reconstruct past concentrations of atmospheric CO$_2$ to understand the drivers and responses of climate change over orbital and geological time scales. Unlike many environmental proxies where it is difficult to assess the accuracy of the resulting reconstructions (e.g. for sea surface temperature), the boron isotope pH/CO$_2$ proxy can directly be compared with the ice core CO$_2$ records, i.e. the West Antarctic ice sheet divide (Ahn et al., 2012), the EPICA (European Project for Ice Coring in Antarctica) dome Concordia ice core record (Siegenthaler et al., 2005; Lüthi et al., 2008; Bereiter et al., 2015), and the Vostock ice core record (Petit et al., 1999). This comparison of CO$_2$ over the last 800 kyr provides a very powerful test of proxy accuracy. Several past intervals have been studied to test the boron isotope proxy in this way

44 (Sanyal et al., 1995; Foster, 2008; Hönisch and Hemming, 2005; Henehan et al., 2013; Raitzsch et al.,
45 2018).

46 Given the success of these comparisons, the boron isotope proxy has been used to investigate the
47 interaction between CO2, the ocean carbon cycle and climate beyond the reach of the ice cores, such as
48 during the Mid-Pleistocene transition (Hönisch et al., 2009; Chalk et al., 2017; Dyez et al., 2018), the
49 Pliocene (Martinez-Boti et al., 2015, de la Vega et al., 2020), the Miocene (Foster et al., 2012; Greenop
50 et al., 2014, Guillermic et al., 2022), the Eocene (Anagnostou et al., 2016, 2020; Harper et al., 2020),
51 Paleocene-Eocene boundary (Penman et al., 2014; Gutjahr et al. 2017) and the Cretaceous-Palaeogene
52 boundary (Henehan et al., 2019). Application of the boron isotope proxy is however complicated by the
53 need for: (i) an empirical species-specific calibration of $\delta^{11}B_{foraminifera}$ to $\delta^{11}B_{borate}$ in the pH expression
54 (Henehan et al., 2013, 2016, hereafter $\delta^{11}B_{foram-borate}$ calibration), sometimes including extinct species
55 for deep-time reconstruction; (ii) $\delta^{11}B$ of seawater ($\delta^{11}B_{sw}$), temperature and salinity in the past to
56 calculate pH from $\delta^{11}B$; and (iii) a second carbonate parameter (typically total alkalinity, dissolved
57 inorganic carbon, DIC, or calcite saturation state) to convert pH to CO_2. While these variables do not
58 influence the magnitude of uncertainty equally in all time intervals, assessment of the boron-based
59 reconstructions against existing ice-core records is a powerful test of the proxy's accuracy.
60

61 Recently, Hain et al. (2018) suggested that the radiative forcing from CO_2 change (ΔF_{CO2}) is linearly
62 related to pH change (ΔpH) of equilibrated water of the low-latitude surface ocean when the CO_2 change
63 occurs faster than the residence time of carbon with respect to silicate weathering (e.g., ~1 million years
64 (Myr)). That is, glacial/interglacial CO_2 climate forcing could be estimated directly from reconstructed
65 ΔpH. Given that one of the main priorities for accurate reconstructions of past CO_2 levels is to allow
66 determinations of climate sensitivity, defined as the temperature response to a radiative forcing –
67 typically a doubling of CO_2 with associated slow and fast feedbacks (e.g. Rohling et al., 2013, 2018) –
68 this recognition may provide a useful shortcut. Climate forcing is a perturbation of the planet's energy
69 balance averaged over the planet (Hansen et al., 2008) and CO_2 forcing, ΔF_{CO2} expressed in $W.m^{-2}$, at a
70 given time can be written as:

71 $$\Delta F_{CO2} \cong \alpha_{2xCO2} * \frac{\Delta \log_{10} CO_2}{\log_{10} 2} \ (1)$$

72 where α_{2xCO2} is the sensitivity of the radiative balance per doubling of CO_2, and $\Delta\log_{10}CO_2$ is the CO_2
73 change over time expressed in terms of how many 10-foldings of proportional (not absolute) CO_2
74 change (Hain et al., 2018).

76 By considering basic equilibrium reactions of carbon species, $\Delta\log_{10}CO_2$ can be derived and expressed
77 as:

79 $$\Delta \log_{10} CO_2 \cong \Delta\log_{10} DIC + \Delta pK_0 + \Delta pK_1 - \Delta pH \ (2)$$

81 Hain et al. (2018) showed that the terms $\Delta\log_{10}DIC$ and $\Delta pK_0 + \Delta pK_1$ are small and that $\Delta\log CO_2$ can
82 therefore simply be expressed as :

84 $$\Delta \log_{10} CO_2 \cong -\Delta pH \ (3a)$$

86 $$\Delta F_{CO2} \cong -\frac{\log_{10} 2}{\alpha_{2xCO2}} \Delta pH \ \cong \ -12.3\Delta pH \ (3b)$$

88 To assess the uncertainty of this approximate -1:1 $\Delta\log_{10}CO_2/\Delta pH$ relationship Hain et al. (2018)
89 considered three different end-member causes to compute the accurate $\Delta\log_{10}CO_2/\Delta pH$ relationship:
90 (1) DIC addition/removal yields a slope of -1.3:1 (relative to the basic formalism), (2) $CaCO_3$
91 addition/removal (e.g. precipitation/dissolution, riverine input) yields a slope of -0.9:1, and (3)
92 warming/cooling yields a slope of -1.1:1. That is, even if ΔpH was known exactly this range of
93 plausible slopes results in estimated $\Delta\log_{10}CO_2$ and ΔF_{CO2} that are systematically biased by -10% for
94 change caused purely by $CaCO_3$ variations or +30% for change purely caused by DIC variations

95   relative to the approximate -1:1 $\Delta\log_{10}CO_2/\Delta pH$ relationship. While introducing such structural
96   uncertainty in the estimation of ΔF_{CO2} is a concern, this approach eliminates the need to assume a
97   second carbonate system parameter and the uncertainty incurred thereby. An estimate of $\delta^{11}B_{sw}$ is still
98   needed to reconstruct pH based on the boron isotope proxy system (Foster and Rae, 2016) but
99   estimated pH change (i.e., ΔpH) is much less sensitive to error in assumed $\delta^{11}B_{sw}$ than is absolute pH
100 (Hain et al., 2018). An important caveat to estimating ΔF_{CO2} directly from ΔpH is that the intercept of
101 the $\Delta\log_{10}CO_2/\Delta pH$ relationship can change with silicate weathering carbon cycle dynamics thought
102 to be important on a million-year timescale, such that the approach is applicable for orbital timescale
103 variability and short-term shifts but not for long-term trends in ΔF_{CO2}. Therefore, the orbital timescale
104 ice age cycles of atmospheric CO_2 reconstructed from air occluded in Antarctic ice cores offer a
105 unique opportunity to determine the $\Delta\log_{10}CO_2/\Delta pH$ relationship observationally and compare to
106 theory. Furthermore, given the principal drivers of the glacial-interglacial CO_2 cycles (e.g. change in
107 water masses, sea-ice cover, the soft tissue pump, the solubility pump, the $CaCO_3$ counter pump and
108 the disequilibrium pump; see Sigman et al., 2010; Hain et al., 2010, 2014 for a full review), will
109 impact the $\Delta\log_{10}CO_2/\Delta pH$ relationship in different ways, comparing the slope of the regressed
110 $\Delta F/\Delta pH$ line from data to theoretical endmembers (temperature, DIC, $CaCO_3$) could allow the
111 primary controlling mechanisms during Glacial-Interglacial (G-IG) cycles to be deciphered.
112
113 In light of these recent advances, our aims here are twofold. First, we extend previous ice-core validation
114 studies (Foster, 2008; Henehan et al. 2013; Chalk et al., 2017) and test the extent to which boron
115 isotopes reconstruct CO_2 faithfully when current methods and assumptions are applied. In contrast to
116 most previous studies, we use two deep ocean sites and present $\delta^{11}B$ and CO_2 data at high temporal
117 resolution (1 sample every ~3 to 6 kyr). This enables: (i) a thorough test of the assumptions typically
118 made including the central tenet of atmospheric CO_2 proxies that surface ocean CO_2 remains in
119 equilibrium with the atmosphere over time at any given site, (ii) an evaluation of the overall uncertainty
120 of the proxy; (iii) an evaluation of the influence of variable foraminiferal preservation on the accuracy
121 of the CO_2 reconstructed; and (iv) a refinement of a number of the input assumptions and uncertainties,
122 including the $\delta^{11}B_{borate-foram}$ calibration. Second, we evaluate the approach of Hain et al. (2018) and
123 assess the robustness of pH change to not only provide insights into the magnitude of climate forcing
124 from CO_2 change, but also the ability of this approach to provide insights into the causes of CO_2 change
125 over glacial-interglacial cycles.
126

127 **2.   Methods.**

128 **2.1   Core location and oceanographic setting.**

129 To accurately reconstruct atmospheric CO_2 with the $\delta^{11}B$-CO_2 proxy, it is essential to measure $\delta^{11}B$ in
130 foraminifera from locations where the CO_2 flux between the ocean and the atmosphere is in near
131 equilibrium. We therefore target regions of the ocean where the water column is stratified and
132 oligotrophic as these regions are most likely to attain this condition (Takahashi et al., 2009). Here,
133 following previous studies (Foster, 2008, Henehan et al., 2013; Chalk et al., 2017), we report and add
134 new data from ODP Site 999 (Figure 1, 12.75°N, 78.73°W, water depth 2827 m, sedimentation rate 3.7
135 cm/ky) in the Caribbean and supplement this well studied site with samples from ODP Site 871 in the
136 Western Pacific (5.55°N, 172.35°E, water depth 1255m, sedimentation rate ~1 cm/ky). The sediments
137 studied at ODP Site 871 are shallowly buried and the site today features a deep thermocline and is
138 located off the equator, hence they are unlikely to be influenced by significant equatorial upwelling
139 (Dyez and Ravelo, 2013, 2014). These two sites show a minor annual mean disequilibrium of +12 ppm
140 (range ~0 to ~30 ppm, Takahashi et al., 2009) for ODP Site 871, and +21 ppm (Olsen et al., 2004;
141 Foster, 2008) for ODP Site 999. These disequilibria are used to correct our CO_2 data derived from $\delta^{11}B$
142 and are assumed to be constant throughout the entire record presented here (with an uncertainty of $\pm$ 10
143 ppm).
144

145 Whilst we recognised that both sites have a minor disequilibrium, this is often a necessary
146 compromise as areas of the ocean that are in strict equilibrium with the atmosphere are often located
147 in the middle of oceanic gyres and tend to have deep sediments located under the lysocline, have a
148 low sedimentation rate and/or are outside the preferred geographic habitat of *G. ruber*. Furthermore,
149 we present surface $\delta^{18}O$ and $\delta^{13}C$ (site 871) and temperature (both sites) from *G. ruber* that provide
150 insight into the potential influence of upwelling (see section 4.2.2) at these locations. Recent Earth
151 System Model (IPSL-CM5A-MR) outputs (Gray and Evans, 2019) also show that relative pH
152 difference at our core sites between the last glacial maximum (LGM) and the pre-industrial (PI),
153 compared to the ocean average pH difference are close to 0, giving confidence that changes in local
154 disequilibrium are unlikely to drive large changes in our CO_2 reconstructions (at least during the last
155 glacial period).
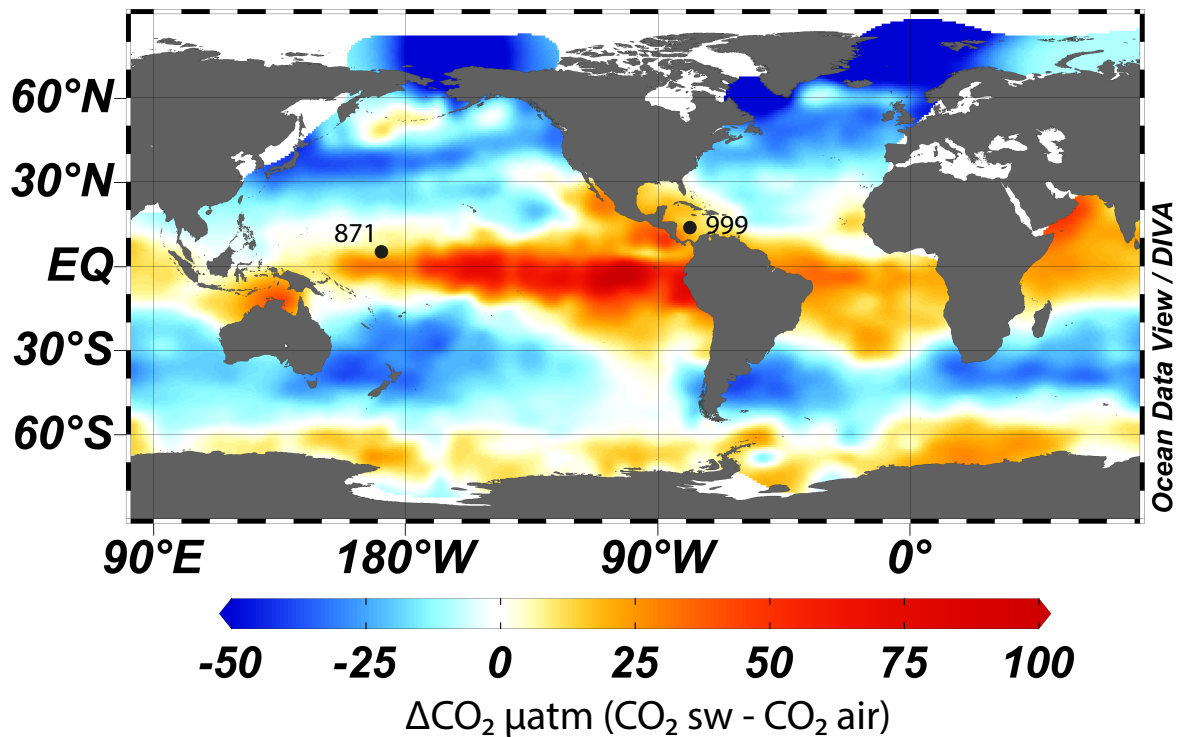
156
157
158
159 Figure 1. Map of air-sea CO_2 disequilibrium (seawater – air) in ppm and location of ODP sites used in this study.
160 CO_2 data from Takahashi et al. (2009). The map was made with Ocean Data View (Schlitzer, 2022).

161 **2.2   Samples.**

162 *2.2.1 Sample selection and preparation.*

163 Samples of deep-sea sediment from our two study sites were taken at 6cm (~3ky) and 10cm (~6ky)
164 resolution at ODP 871 and 999 respectively. Around 1-2 mg of the foraminifer (between 120 and 200
165 individuals) from the species *Globigerinoides ruber sensu stricto white* (here after *G. ruber ss*) were
166 hand-picked from the size fraction 300-355 μm for a target of 10 to 20 ng of boron. *G. ruber ss* was
167 chosen here because it is readily identified, is abundant throughout our chosen time interval and a
168 $\delta^{11}B_{foram-borate}$ calibration that accounts for vital effects is available from culture, plankton tows and core-
169 top samples (Henehan et al., 2013). It is also known to live in the upper surface of the ocean with a
170 relatively small depth range (Rebotim et al., 2017) which prevents significant influence of deeper more
171 remineralised CO_2-rich waters on the measured $\delta^{11}B$. The morphotype *G. ruber sensu lato* (hereafter
172 *G. ruber sl*) has slightly different morphology (Aurahs et al, 2011; Carter et al., 2017) and is thought to
173 live in deeper water compared to *G. ruber ss* (Wang, 2000). The morphotype *G. ruber sl* was also hand

174   separated and analysed at lower resolution at ODP 871 to monitor any change over time in morphotype
175   differences in $\delta^{11}B$ that could result from different habitats. For similar reasons, carbon and oxygen
176   isotopes ($\delta^{18}O$ and $\delta^{13}C$) were also measured on *G. ruber ss* and *sl* for comparison on the whole record
177   at ODP 871. For this, around 10 individuals of *G. ruber* per sample were picked, their shells gently
178   broken open and mixed and then a 100 μg aliquot of the homogenised carbonate was measured using a
179   Thermo KIEL IV Carbonate device at the University of Southampton, Waterfront Campus. . While this
180   number of specimens is lower than classically done for $\delta^{18}O$ and $\delta^{13}C$ analysis, it provides power for
181   the identification of species-specific preferential diagenetic alteration, which may have occurred in the
182   sediment and it was sometimes necessary due to the scarcity of some of the *G. ruber* spp morphotypes.
183

184   *2.2.2   Age constraints.*

185   Samples were taken from 1.5 to 5 metres below sea floor (mbsf) for ODP 871 and from 9 to 21 mbsf
186   for ODP 999. Sample age at Site 871 was initially determined from sample depth using published age
187   models (Dyez and Ravelo, 2013). At Site 999, the age was determined by developing a new
188   *Cibicidoides wuellerstorfi* benthic $\delta^{18}O$ record. The initial age model at Site 871 was refined by
189   measuring $\delta^{18}O$ on the benthic species *Uvigerina peregrina* (50 μg of 3-5 mixed, crushed, and
190   homogenised specimens) measured on a Thermo KIEL IV Carbonate device at the University of
191   Southampton, Waterfront Campus. These new $\delta^{18}O$ data (Figure 2) were then tuned to the benthic
192    $\delta^{18}O$ LR04 stack (Lisiecki and Raymo, 2005) using Analyseries (Paillard et al., 1996). A correction of
193   +0.47 was applied to the $\delta^{18}O$ *Cibicidoides wuellestorfi* at ODP Site 999 following Marchitto et al.
194   (2014).

195

196   *2.2.2   Fragment counts.*

197   Foraminifera fragment counts were conducted on ODP Site 871 to monitor variations in carbonate
198   preservation. Samples were sub-sampled using a splitter (in order to maintain homogeneity) and poured
199   onto a picking tray. The fragmentation index (FI) was calculated following the approach of Howard and
200   Prell (1994) and Berger (1970) where percentage fragment is defined as:
201

202    $$FI = 100 * \frac{number\ of\ fragments}{number\ of\ fragments + number\ of\ whole\ tests} \quad (4)$$

203
204   Counts of whole intact grains and fragments of grains were conducted three times and averaged. The
205   standard deviation (1σ) of the fragmentation index is 1.69. This approach followed that used in an early
206   study at ODP Site 999 (Schmidt et al. 2006) ensuring that the datasets between the two sites are
207   comparable.

208   *2.2.3   Boron separation.*

209   The hand separated foraminifera tests for boron isotope analysis were broken open, detrital clay was
210   removed, and oxidatively cleaned and leached in a weak acid to obtain a primary carbonate signal
211   using established methods (Barker et al., 2003). Samples were then slowly dissolved in ~ 100 μl
212   0.5M HNO_3 added to 200 μl of MQ water. Dissolved samples were then centrifuged for 5 minutes to
213   separate any remaining undissolved contaminants (e.g. silicate grains, pyrite crystals) and transferred
214   to screw top 5 ml Teflon pots for subsequent boron separation. An aliquot equivalent to 7% of each
215   sample was kept for elemental analysis and transferred to acid cleaned plastic vials in 130 μl 0.5M
216   HNO_3. Samples were purified for boron using anion exchange column chemistry method prior to
217   isotope analysis as described elsewhere (Foster, 2008). A total procedure blank (TPB) was conducted
218   for each batch of samples and typically ranged from 0 to 100 pg which represents a blank contribution
219   of up to 2.3% (for samples containing ~10-20 ng of boron). Most samples had a TPB below 40 pg

220   and were not corrected. Two batches had a TPB of 70 and 100 pg for which we corrected using a
221   long-term median TPB δ^{11}B value of -7.27‰ from the University of Southampton. This represents a
222   δ^{11}B correction of 0.1 to 0.7 ‰.

2.3 Analytical techniques

224   Boron isotope analyses were performed on a ThermoScientific Neptune multi collector inductively
225   coupled plasma mass spectrometer (MC-ICPMS) with 10^{12} Ω amplifier resistors using a standard-
226   sample bracketing routine with NIST 951 boric acid standard (following Foster et al. 2013 and Foster,
227   2008). Elemental analysis was performed on each dissolved sample using a ThermoScientific Element
228   inductively coupled plasma mass spectrometer (ICPMS). All analyses were carried out at the University
229   of Southampton, Waterfront Campus (following Foster, 2008 and Henehan et al., 2015). Element to
230   calcium ratios were measured with ^{43}Ca and ^{48}Ca and measured against in house mixed element
231   standards. Elemental ratios measured included: B/Ca, Mg/Ca, Al/Ca, Mn/Ca, Sr/Ca. Based on the
232   reproducibility of our in-house standards, the uncertainty for most elemental ratios is ~ 5% (at 95%
233   confidence).

2.4 Constraints on δ^{11}B-derived pH and CO_2.

235   *2.5.1   From $\delta^{11}B$ to pH.*

236   Seawater pH is related to the boron isotopic composition of dissolved borate ion by the following
237   equation:

$$pH = pK_B - \log\left(-\frac{\delta^{11}B_{sw} - \delta^{11}B_{borate}}{\delta^{11}B_{sw} - a_B * \delta^{11}B_{borate}(a_B - 1)}\right) \ (5)$$

241   where the isotopic fractionation factor α_B between B(OH)$_3$ and B(OH)$_4^-$, is 1.0272 as determined by
242   Klochko et al. (2006) and the δ^{11}B of seawater is 39.61 ‰ (Foster et al., 2010) for both sites and kept
243   constant throughout the record due to the long residence time of boron (10-20 Myrs, Lemarchand et al.
244   2002).

247   The sea surface temperature (SST) values necessary to calculate pK_B in equation (5) were determined
248   at both sites using the Mg/Ca of *G. ruber* (Dyez and Ravelo, 2013) including a depth-dependent
249   dissolution correction for each site (following Dyez and Ravelo, 2013 for Site 871 and Schmidt et al.,
250   2006 for Site 999) and a pH correction using the iterative approach of Gray and Evans (2019) to account
251   for the observed pH effect on Mg/Ca in *G. ruber* producing higher apparent sensitivity of Mg/Ca during
252   glacial cycles (Gray et al., 2018).

254   Mg/Ca was corrected for depth-dependent dissolution at Site 871 using the following equation (Dyez
255   and Ravelo, 2013):

$$\frac{Mg}{Ca}(corrected) = \frac{Mg}{Ca}(measured) + 0.26 * depth + 0.52 \ (6a)$$

257   Mg/Ca from Site 999 was corrected following Schmidt et al. (2006):

$$\frac{Mg}{Ca}(corrected) = \frac{Mg}{Ca}(measured) + 0.66 \ (6b)$$

259

260   To evaluate the effect of various Mg/Ca treatment on temperature and calculated CO_2, we performed
261   seven sensitivity tests (Table S1) with Mg/Ca-derived SST using the calibrations of: (1) Gray et al.
262   (2018) temperature-dependent only (global calibration), (2) Gray and Evans (2019) with a pH
263   correction; (3) Gray et al. (2018) temperature-dependent with Mg/Ca corrected for depth-dependent
264   dissolution; (4) Gray and Evans (2019) with Mg/Ca corrected for depth-dependent dissolution and pH
265   correction; (5,6) Anand et al. (2003) with and without a depth correction; and (6) with temperature
266   kept constant (26°C).

267   The differences in SST and resulting CO_2 can be substantial (Figure S1, Table S2): up to 6 degrees
268   and ~50 ppm, respectively, between the Gray et al. (2018) calibration uncorrected for pH and the
269   Anand et al. (2003) calibration corrected for dissolution. We have chosen the Mg/Ca treatments that
270   accounts for pH effect on Mg/Ca and yields the closest agreement between coretop at both sites and
271   modern temperature from Glodap v2 (Lauvset et al., 2022) This treatment is with a pH correction and
272   Mg/Ca corrected for depth-dependent dissolution. Choosing this approach is justified considering (1)
273   the strong offset between Anand et al. (2003) multi-species Mg/Ca-Temperature calibration and the
274   more recent *G. ruber* compilation of Gray et al., (2018); (2) the effect of pH correction as shown in
275   Gray et al., (2018) and Gray and Evans (2019); (3) the suggested influence of dissolution on Mg/Ca
276   (Dyez and Ravelo, 2013; Schmidt et al., 2006) and (4) the better agreement between coretop and
277   modern SST at each site when using a pH and depth correction (Figure S1).

278   The salinity (S) that is used in the expression of pK_B is kept constant for both sites (35) due to the very
279   minor effect of salinity on calculated pH/CO_2 (1 salinity unit changes pH by 0.006).
280
281

282   *2.5.2   From pH to CO_2.*

283   Calculating CO_2 from boron isotope derived pH is dependent on the determination of a second
284   parameter of the carbonate system. Here we use the modern value of total alkalinity (TA) at each site:
285   2279 and 2350 µmol/kg at ODP 871 and ODP 999, respectively (Shipboard Scientific Party, 1993;
286   Takahashi et al., 2009). Following Chalk et al. (2017), these values were kept constant throughout the
287   whole record. To account for any variations in alkalinity, a generous uniform (i.e. equal likelihood of
288   values within the range of uncertainty) uncertainty of 175 µmol/kg, distributed equally on either side of
289   the central value, is applied. This range in TA encompasses the likely range in this variable on glacial-
290   interglacial (e.g. Toggweiler, 1999; Hain et al., 2010; Cartapanis et al., 2018) or longer timescales
291   (Hönisch et al. 2009), and its adoption means the local TA record is not tied to a global sea-level record
292   as has been practiced previously. We avoid drawing this link because the ~+3% (+68µmol/kg)
293   concentration increase of solute alkalinity occurring from sea-level lowering during the last glacial
294   maximum may not have been the dominant driver of ocean alkalinity change (Boyle, 1988a/b; Sigman
295   et al., 1998; Toggweiler, 1999; Hain et al., 2010; Cartapanis et al., 2018). By assuming a uniform
296   distribution for TA we avoid imposing a temporal evolution to this variable because evolution of TA
297   through a glacial cycle is uncertain and is unlikely to be simply a function of sea-level or salinity (e.g.
298   Dyez et al. 2018) due to the effect of carbonate compensation.

299   The surface water CO_2 is then calculated as (Zeebe and Wolf-Gladrow, 2001):
300
301

302 $$CO_2 = \frac{TA - \frac{K_B * B_T}{K_B + [H^+]} - \frac{K_W}{[H^+]} + [H^+]}{\frac{K_1}{[H^+]} + \frac{2K_1 K_2}{[H^+]^2}} \quad (7)$$

303
304   where TA is the total alkalinity, K_B the equilibrium constant of boron species in seawater, B_T the
305   concentration of boron in seawater (432.6 µmol/kg, Lee et al., 2010), $[H^+]$ the concentration of H^+
306   determined from pH = - log $[H^+]$, K_W the dissociation constant of water (function of T, S and pressure),

307 K_1 and K_2 the first and second dissociation constants of carbonic acid (function of T, S and pressure,
308 Luecker et al., 2000). The estimate of atmospheric CO_2 includes site-specific offsets relative to
309 reconstructed surface water CO_2 to account for observed local disequilibrium (+21 ppm and +12 ppm
310 at ODP Sites 999 and 871, respectively).

311 **2.6 Uncertainty.**

312 *2.6.1 Analytical uncertainty.*

313 The uncertainty on the measured $\delta^{11}B$ is expressed as the external uncertainty which includes
314 instrumental error and chemical separation of the sample (see a detailed discussion in John and Adkins,
315 2010). This was determined empirically by long-term repeat measurements of JCp-1 subject to the same
316 chemical purification as our foraminiferal samples. As discussed by Rae et al. (2011) this uncertainty
317 is dependent on the intensity of the ^{11}B signal and is expressed here by the following relationship defined
318 during the duration of this study at the University of Southampton (Anagnostou et al., 2019), for ^{11}B
319 intensities <0.54V:

320 $$2\sigma = 129600\ e^{-212\ \times\ [^{11}B]} + 0.3385\ e^{-1.544\ \times\ [^{11}B]} \text{ (8)}.$$

321
322 where $[^{11}B]$ is the intensity of ^{11}B signal in volts. The $\delta^{11}B$ uncertainty for ^{11}B intensities > 0.54V is
323 0.15‰ (at 95% confidence).
324

325 *2.6.2 pH and CO_2 uncertainty.*

326 The CO_2 uncertainty we report was calculated with a Monte Carlo simulation (10, 000 realisations) in
327 order to fully account for the uncertainty in all variables used in the calculation of pH and CO_2 (σ_{CO2}
328 $_{\delta11B\text{-derived}}$). The shape of the uncertainty distribution sampled is either normally distributed (for
329 temperature, salinity and $\delta^{11}B$) or uniform (for alkalinity, as discussed above). The maximum
330 probability of all realisations was used as the central value for CO_2 and an error envelope at 1 and 2σ
331 was calculated based on the 68% and 95% distribution of the realisations.
332

333 *2.6.3 Uncertainty on the CO_2 offset.*

334 To constrain the offset between $\delta^{11}B$-derived CO_2 and ice core CO_2, each sediment age is compared to
335 the ice core CO_2 record by interpolation of the record of highest resolution (in this case the $\delta^{11}B$ record
336 onto the ice core compilation). To fully account for age uncertainty when interpolating the sediment
337 age to the well-dated ice core record, a distribution of the ice core data was calculated within the 4σ
338 uncertainty of the $\delta^{11}B$ age and weighed by the respective likelihood based on the age difference
339 between ice core and sediment core.
340
341 The CO_2 offset (or residual) is defined by:
342
343 $$\text{Offset}_{CO2} = CO_{2\ \delta11B\text{-derived}} - CO_{2\ \text{ice}} \text{ (9)}$$
344
345 The uncertainty on this offset (σ_{offset}) accounts for the uncertainty of the interpolated ice core CO_2
346 ($\sigma_{CO2.\text{interpol}}$) and the one of the $\delta^{11}B$-derived CO_2 ($\sigma_{CO2.\delta11B\text{-derived}}$), such as :
347
348
349 $$\sigma_{\text{offset}} = \sqrt{\sigma^2_{CO2.\text{interpol}} + \sigma^2_{CO2.\delta11B-\text{derived}}} \text{ (10)}$$

2.7 The relationship between $\delta^{11}B$ -derived pH and ΔF_{CO2}.

The linear relationships between the relative CO_2 forcing ΔF_{CO2} and pH are determined with a York regression (York et al., 2004) that accounts for the uncertainty in both the independent and dependent variable (i.e. x and y axes). The ice core CO_2 interpolation used to calculate ΔF_{CO2} and uncertainty is determined as described in section 2.6.3 (Hain et al., 2018).

2.8 Optimising the *G. ruber* $\delta^{11}B$ borate-foraminifera calibration.

An optimised *G. ruber* calibration was obtained by minimising the root mean square error (RMSE) of the average offset between $\delta^{11}B$-derived CO_2 and ice core CO_2. The steps are illustrated in Figure S2. In order to optimise the calibration, 10,000 simulations of $\delta^{11}B_{borate}$ and $\delta^{11}B_{foraminifera}$ from the calibration of Henehan et al. (2013) were performed within their normally distributed uncertainty (1σ), from which we defined the same number of linear models each including their slope and intercept. Then, we calculate the equilibrium pH and resultant equilibrium $\delta^{11}B_{borate}$ from ice core CO_2 and the assumed constant TA at each core site. The $\delta^{11}B_{borate}$ from the 10,000 linear models is then calculated and the difference to the ice core-derived $\delta^{11}B_{borate}$ is determined. The linear model calibration that yields the minimum RMSE between these two borate variables defines the new $\delta^{11}B_{borate-foram}$ calibration. To assess the effect of $\delta^{11}B$ records from different sites we performed this exercise using the combined records (from both sites 999 and 871), 999 only and 871 only (Figure S3) and show that using a record from one particular site or the combination of sites yields similar CO_2 offsets (Table S3) and so here we use the results from the combined sites. Unless indicated otherwise, to preserve a degree of independence, the pH results presented in this study are calculated with the published calibration (Henehan et al., 2013), and the results with the optimised calibration presented in section 4.2.6.

3   Results.

3.1   Temperature and fragment counts.

The SST at ODP Sites 999 and 871 show a cyclicity that agrees with the well-known glacial interglacial cycles of the late Pleistocene (Figure 2). The SST determined from *G. ruber sl* (red filled circles, Figure 2B) at Site 871, show equal or cooler temperatures (by 1-2 °C) than *G. ruber ss* (black filled circles). The fragmentation index (Figure 2D) at ODP 871 range from 20 to 50 % and follow the well-documented "Pacific style" dissolution cycles (Sexton and Barker, 2012) with well-preserved carbonate (low fragments) during glacials and less well-preserved carbonates (higher fragments) during interglacials. The percentage sand typically anticorrelates with fragmentation counts at both sites, although it is less clear at ODP 999, perhaps due to the shorter record available. Fragmentation counts reach maxima at ODP 999 of 20 % during interglacials and up to 50 % during marine isotope stage MIS 11 which is concomitant with the mid-Brunhes dissolution interval (MBDI, Barker et al., 2006). The fragmentation counts at ODP 871 show no substantive anomaly during the MBDI.
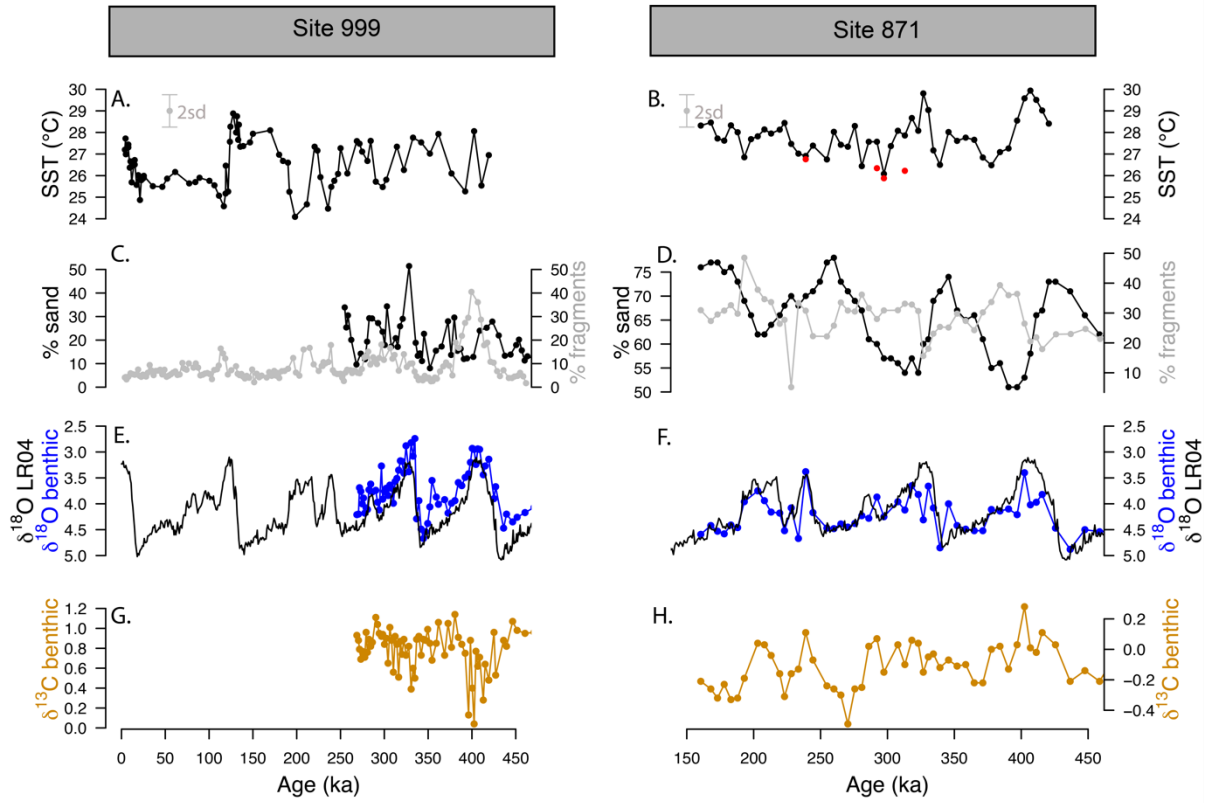
Figure 2. Mg/Ca derived temperature, coarse fraction (sand), fragmentation and benthic $\delta^{18}O$ and $\delta^{13}C$ at ODP sites 999 and 871. **A, B:** Temperature at ODP 999 (from *G. ruber ss*, black, Schmidt et al., 2006 and this study) and ODP 871 (*G. ruber ss*, black, *G. ruber sl*, red, 2sd indicated by the grey error bar). **C, D:** Fragmentation index (light grey, data from Schmidt et al. (2006) for ODP 999) and sand (black line). **E, F:** Benthic *C. wuellestorfi* (Site 999) and *U. peregrina* (Site 871) $\delta^{18}O$ (blue) and LR04 benthic $\delta^{18}O$ stack (black). A correction of +0.47‰ is applied to $\delta^{18}O$ of *C. wuellestorfi* data in order to adjust for species offset. **G, H:** Benthic *C. wuellestorfi* (Site 999) and *U. peregrina* (Site 871) $\delta^{13}C$ (orange).

3.2 pH and CO$_2$ reconstructions.

The $\delta^{11}B$, pH and $\delta^{11}B$-derived absolute CO$_2$ (Figure 3) from Sites 871 and 999, show clear cyclicity related to glacial-interglacial cycles. The CO$_2$ values carry an average uncertainty of ±48 ppm and the mean offset from the ice core CO$_2$ for a combination of the two records is 13±46 (2σ) ppm showing that there is a minor overestimation of CO$_2$ using the boron method yet it agrees on average well within uncertainty. The RMSE of the CO$_2$ offset for the combined record is 26 ppm.

Despite the overall close agreement between $\delta^{11}B$-derived CO$_2$ and ice core-derived CO$_2$, each of our $\delta^{11}B$-CO$_2$ records exhibit some short-lived intervals where the offsets from the ice core record are larger. This is further revealed by the residual CO$_2$ and the identification of the data above the upper quartile (i.e. the upper 25% of the data, Figure S4). Those data do not appear to be randomly distributed and instead occur at ~100 ky, ~220-290 ky and ~390 ky at ODP Site 999, in all three cases during the early stages of the glaciation (except for the MIS 8 glacial at 280ky, Figure S4). The mismatches with the ice core at ODP Site 871 show a similar temporal pattern occurring at ~220 and ~300 and ~ 350-390 ky (i.e. at glacial inceptions).
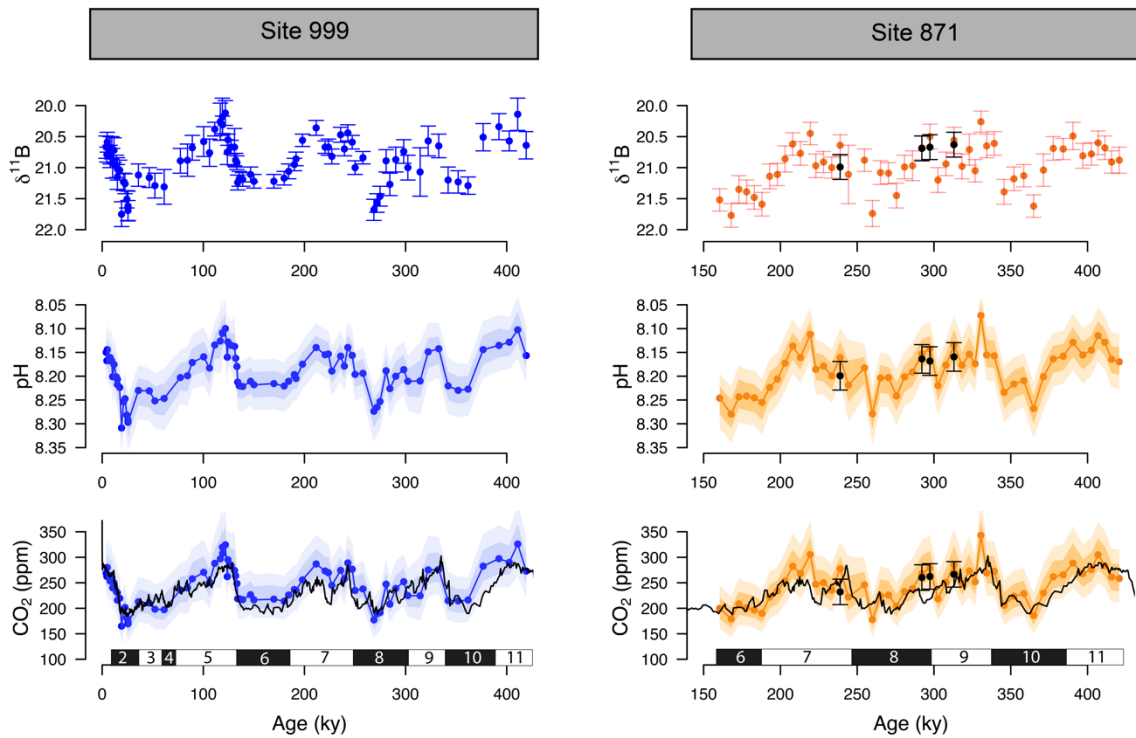
415

416

417

418   Figure 3. δ^{11}B, pH and boron-derived CO_2 at site 999 and 871. δ^{11}B of *G. ruber ss* and *sl* (top row), boron-derived
419   pH (middle row) and CO_2 (bottom row) reconstruction from two core locations: ODP 999 (blue, this study and
420   published data, Foster, 2008; Henehan et al., 2013; Chalk et al., 2017) and ODP 871 (orange, this study). The
421   black line in the CO_2 panels is the composite Antarctic ice core CO_2 record (Bereiter et al., 2015). All δ^{11}B-derived
422   data points are from *G. ruber ss* except black dots at ODP Site 871 measured on *G. ruber sl*. Numbers at the
423   bottom of the CO_2 records represent marine isotope stages (black boxes for glacials and white boxes for
424   interglacials). Note the age scale is different between Sites 999 and 871.

425

426   **3.3 Contrasting δ^{11}B between morphotypes.**

427   Within error, the few measurements of δ^{11}B *G. ruber sl* at ODP 871 all agree with δ^{11}B *G. ruber ss*
428   (Figure 3) albeit the δ^{11}B of *G. ruber sl* are higher than *G. ruber ss* for all 4 data pairs available. The
429   CO_2 derived from *G. ruber sl* (Figure 3) is on average 22 ppm lower than the one derived from *G. ruber*
430   *ss*; though the much lower resolution (n=4) impedes a thorough comparison at this stage. The δ^{18}O and
431   δ^{13}C of both morphotypes were compared for the whole records at ODP 871 (Figure S5) and a cross-
432   plot shows a moderate to good agreement between *G. ruber ss* and *sl* (r^2=0.55 and 0.22 for δ^{18}O and
433   δ^{13}C respectively, Figure S6). This is in contrast to other studies (e.g. Wang et al., 2000; Steinke et al.,
434   2005) that show δ^{18}O in *G. ruber sl* to be systematically higher.

435   **3.4 Relationship between δ^{11}B-pH and CO_2 forcing from the ice core.**

436   A cross plot of δ^{11}B-derived pH CO_2 forcing from the ice core record for each of our marine core study
437   sites is shown in Figure 4 and is compared to the theoretically-derived approximate $\Delta FCO_2/\Delta pH$
438   relationships as adopted by Hain et al. (2018): -1:1 W/m^2 (dashed black line); $CaCO_3$ addition/removal
439   (-0.9:1 W/m^2 plain yellow line); DIC addition/removal (-1.3:1 W/m^2 dotted-dashed blue); and
440   warming/cooling temperature forcing (-1.1:1 W/m^{2,} dashed red). Our analysis includes full propagation
441   of uncertainty in pH, in contrast to Hain et al. (2018) who considered only the reported uncertainty of
442   δ^{11}B$_{borate}$ in their validation exercise. In both cases the uncertainty in ΔF_{CO2} accounts for the error in

443 interpolation arising when comparing age-uncertain $\delta^{11}B$-derived pH with ΔF_{CO2} from the well-dated
444 and high-resolution ice core CO_2 record (see methods 2.7 and 2.6 for details). This treatment of ΔF_{CO2}
445 uncertainty is dominated by the spread of ice core CO_2 data points within the $\delta^{11}B$ age uncertainty. The
446 data are fitted with a York-type regression (thin black line; York et al., 2004) where the grey envelope
447 represents the uncertainty of the linear relationship that best represents the data (i.e., the envelope is not
448 the prediction interval), considering the uncertainty in pH and ΔF_{CO2}. The regressed slope is $\Delta F/\Delta pH =$
449 $- 17.2 \pm 1$ W/m^2 (-1.4:1 relative to basic formalism) and shows a good agreement with the theoretical
450 temperature and DIC driven relationships.

451 The effect of the uncertainty assigned to pH (fully propagated or using the measurement uncertainty of
452 the boron isotope) on the regressed slope is shown in Figure S7. The slope of the York regression when
453 using the uncertainty from $\delta^{11}B$ only, as in Hain et al. (2018), shows a close agreement with the basic
454 formalism, with a slope of $\Delta F/\Delta pH = - 13.7 \pm 0.3$ W/m^2, (-1.1:1 relative to the basic formalism) but
455 with a unsatisfactory goodness of fit (mean squared weighted deviation, mswd) of 5.3, whereas
456 propagating the full pH uncertainty based on our iterative Monte-Carlo simulations improves goodness
457 of fit to ~0.9 at a $\Delta \log_{10}CO_2/\Delta pH$ of -1.4:1 (Figure 4).

458

459
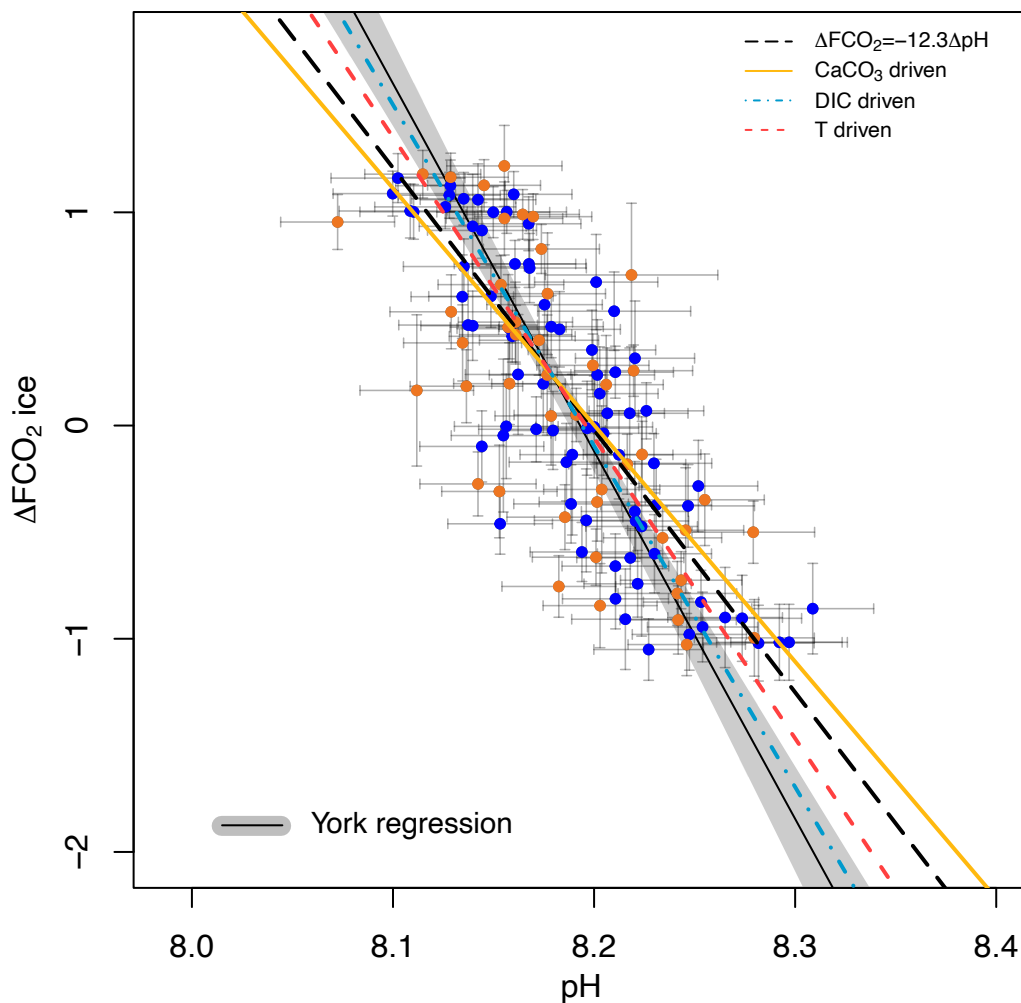
462 Figure 4. Ice core based ΔFCO_2 (CO_2 forcing) vs. $\delta^{11}B$-based pH for ODP 999 (blue filled circles, this study and
463 published data from Foster, 2008; Henehan et al., 2013; Chalk et al., 2017) and 871 (orange filled circles). The
464 lines show the relationship between ΔFCO_2 and pH for the simplified formalism (see method) $\Delta FCO_2 = -12.3\Delta pH$
465 (black dashed line), and when driven by changes in DIC only (blue, $\Delta F/\Delta pH = -16$ W/m^2), $CaCO_3$ (yellow,
466 $\Delta F/\Delta pH = -11.1$ W/m^2) and temperature T (red, $\Delta F/\Delta pH = -14.1$ W/m^2). The York regressed line (black line and
467 grey shade) falls close to the DIC-driven line (blue).

4. Discussion.

4.1 Cyclicity in foraminifera preservation.

470 Percentage fragments and sand fraction (> 63μm) at both studied core sites are anticorrelated and show
471 a clear cyclicity, with better preservation of carbonates during glacial periods (Figure 2). The
472 anticorrelation is clearer at ODP Site 871 where we have the longest record (Figure 2). Preservation in
473 the Pacific (Farrell and Prell, 1989) show improved (poorer) preservation during glacial (interglacial)
474 and this pattern seems to have originated after the mid Pleistocene transition (Sexton and Barker, 2012).
475 The origin of these cycles could be a combination of enhanced ventilation during glacials in the Pacific
476 (Sexton and Barker, 2012), or increased burial due to enhanced global alkalinity following a decrease
477 in burial in the Atlantic (Cartapanis et al., 2018). However glacial periods seem to have been
478 accompanied by a diminution in oxygenation in the deep Pacific (Anderson et al., 2019) that may have
479 also impacted preservation.
480
481 The observation that the fragmentation records of sites 999 and 871 covary is likely attributable to the
482 different water masses that fill the Caribbean basin relative to the rest of the Atlantic basin. During
483 glacials, the deep Atlantic is filled by nutrient- and carbon-rich corrosive southern sourced waters
484 (Antarctic Bottom Water) with a reduced contribution from the less corrosive, nutrient-poor North
485 Atlantic Deep Water (Oppo and Lehman, 1993) causing calcareous sediments in the deep Atlantic
486 Ocean >2500 m to be less well-preserved during glacials than interglacials. The opposite pattern of
487 dissolution is seen in the Caribbean because shoaling of the northern sourced waters during glacials
488 produces a mid-depth well-ventilated water mass that feeds into the Caribbean through its deepest sill
489 (~1900 m, Johns et al., 2002). Thus the deep Caribbean is filled with less corrosive waters during
490 glacials than interglacials improving the preservation of carbonate during glacials in a similar pattern
491 to a Pacific styled dissolution cycle albeit in response to Atlantic circulation changes. During
492 interglacials, the Northern sourced waters are mixed with corrosive southern sourced waters (Antarctic
493 Intermediate Waters and upper circumpolar deep waters) leading to less well-preserved sediments.

4.2 Causes of offset between $\delta^{11}B$ –derived and ice core CO_2.

495 The $\delta^{11}B$-derived CO_2 record from both of our study sites is in very good agreement with the ice core
496 record, with an average offset for combined both cores of 13±46 (2σ) ppm and corresponding RMSE
497 of 26 ppm. However, the minor CO_2 offsets observed in both records do not appear to be random and
498 tend to fall during the first half of each glacial cycle (Figure S4). In order to have the highest confidence
499 in CO_2 reconstructions using $\delta^{11}B$, this pattern warrants further investigation (see below).

4.2.1 Comparison between morphotypes of G. ruber

501 If as others suggested (e.g. Wang et al., 2000; Steinke et al., 2005; Numberger et al., 2009) *G. ruber sl*
502 and *G. ruber ss* occupied different depth habitats, then inadvertent sampling of the cryptic *G. ruber sl*
503 morphotype might conceivably produce the biases we observe between $\delta^{11}B$-derived CO_2 and
504 atmospheric CO_2 from the ice cores. However, while our Mg/Ca-derived temperatures for *G. ruber sl*
505 and *G. ruber ss* display variable offsets, they are within uncertainty (Figure 2) and our $\delta^{18}O$ and $\delta^{13}C$
506 data for the two morphotypes at ODP 871 show a good agreement with no consistent differences (Figure
507 S5). Thus, while the water column profile of $\delta^{18}O$ and $\delta^{13}C$ can be affected by factors other than

508 temperature, salinity and biological productivity (e.g, carbonate ion effect, Spero et al., 1997), overall,
509 our data suggest that the two morphotypes we analysed shared similar depth habitat preferences.

510 Henehan et al. (2013) found that *G. ruber ss* and *sl* record similar δ^{11}B in core-top sediments, and
511 through necessity, used mixed morphotypes in their culture study. The δ^{11}B-derived pH and CO_2 for *G.*
512 *ruber sl* examined here are consistently higher and lower, than *G. ruber ss* by around +0.02 pH units
513 and -22 ppm CO_2 on average, respectively (Figure 3). This is contrary to expectation if *G. ruber sl* lived
514 in deeper more acidic waters as suggested by other studies (Wang et al., 2000; Steinke et al., 2005), but
515 consistent with some data sets that show that the habitat of *G. ruber ss* and *sl* can vary by location and
516 seems to be dependent on local productivity (Numberger et al., 2009). Other data sets from the Atlantic
517 and Indian ocean nevertheless show similar Mg/Ca between both morphotypes (Gray et al., 2018). We
518 acknowledge that the scarcity of *G. ruber sl* in our samples means that our data set for this morphotype
519 is too small to draw firm conclusions and this warrants further investigation at other study sites.
520 Nonetheless, the closeness of the morphotypes in terms of δ^{11}B and depth habitat throughout our record
521 implies any inadvertent sampling of *G. ruber sl* in the *G. ruber ss* fraction in this study and location
522 would not significantly bias our reconstructions.

523 *4.2.2   Change in upwelling and CO_2 disequilibrium.*

524 ODP sites 871 and 999 are both located today in stratified oligotrophic environments with a deep
525 modern thermocline (base of the thermocline is at ~ 200 and 400 m at ODP 871 and 999, respectively;
526 Olsen et al., 2016). It should be noted, however, that both sites are situated relatively close to regions
527 displaying ΔpCO_2 >40 ppm (Figure 1). However, if local upwelling occurred over the study interval,
528 or if these areas of upwelled water expanded, we would expect these periods to be characterised by
529 relatively low SST, high surface δ^{18}O, and low surface δ^{13}C due to an increased influence of deep
530 colder and more remineralised waters. The identified anomalous intervals in residual CO_2 at ODP 871
531 (e.g at ~210, ~290 ky, Figure 5) show no particular anomaly in planktonic C and O isotopes (Figure
532 S5) or in SST (Figure 2, Figure S8), ruling out significant variations in upwelling at that site. The
533 Mg/Ca-derived SST record of nearby Site MD97-2140 (Figure S8) from the Western Pacific warm
534 pool (de Garidel-Thoron et al., 2005) a location outside of the upwelling from the Pacific cold tongue,
535 confirms this view in that the periods of high CO_2 offset at Site 871 are not associated with relatively
536 cold periods at site MD97-2140. Equally, no SST anomaly was identified at ODP 999 to be coincident
537 with the intervals of high residual CO_2. Foster and Sexton (2014) have also reconstructed CO_2 zonally
538 across the equatorial Atlantic and the Caribbean and showed that while enhanced disequilibrium was
539 detected in the eastern Atlantic, for the last 30 ky at least, Site 999 has remained in equilibrium with
540 the atmosphere. This suggests the CO_2 anomalies revealed in Figure 5 are not the result of enhanced
541 local disequilibrium via sub-surface water mixing. Whilst SST is a first order constraint on upwelling,
542 we acknowledge future constrains are needed using paired proxies of local CO_2, temperature, and
543 productivity to evaluate changes in local CO_2 fluxes.

544 *4.2.3   Partial dissolution.*

545 The CO_2 derived from *G. ruber* δ^{11}B at ODP 999 and 871 appears to show, at first order at least, positive
546 CO_2 offset during periods of high fragmentation (~100, ~210, ~400ky, red filled circles in Figure 5,
547 defined by the upper 25% quantile of fragments) following a "Pacific style" dissolution cycle (better
548 preservation and lower fragmentation during glacial periods). Periods of high fragmentation at ODP
549 Site 999 and 871 correspond to a positive CO_2 offset 65 and 75% of the time respectively, and 35 and
550 25% of the time to a negative or no (i.e. ±10 ppm) CO_2 offset, (note that values ±10 ppm were omitted
551 in the criteria for positive or negative offset). We also note that almost all CO_2 offsets uncertainty (2σ)
552 overlap with the 0 line, hence the percentage of CO_2 offset that are above or below the 0 line should be
553 interpreted with caution.

554
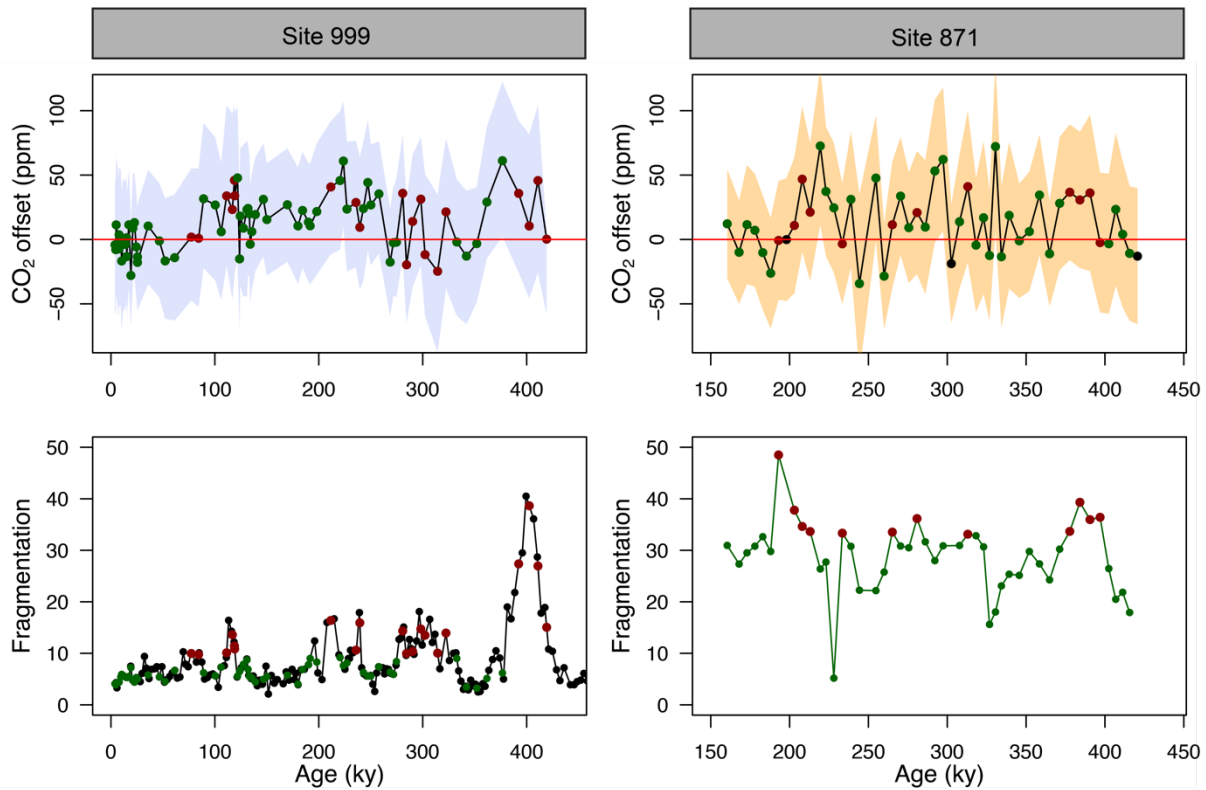
Figure 5. Top panels: CO_2 offset (defined as offset = $CO_{2\_\delta11B\text{-derived}}$ − CO_{2_ice}) for ODP Sites 999 (this study and Chalk et al., 2017) and 871. See text for error bars calculations. Bottom panels: fragmentation index at Site 999 (Schmidt et al., 2006) and 871 (this study). Red dots in the lower panels are the fragments above the upper quartile (and corresponding CO_2 in the upper panel, red dots). Green dots represent periods of low fragments below the upper quartile (and corresponding CO_2 in the upper panel, green dots).

In detail however, a cross-plot of fragment counts and CO_2 offset (Supplementary Figure S9) fitted with a linear regression shows no significant correlation for both core site 999 (r^2=0.06, p=0.03) and 871 (r^2=0.002 , p=0.77). Although it should be noted that this simple linear regression presupposes a linear relationship between the variables and does not account for the significant uncertainty in both CO_2 offset and fragmentation index. In particular, the CO_2 offset carries the uncertainty from the interpolated ice core CO_2 (see methods). Fragment counts at ODP 999 also come with the additional uncertainty related to the interpolation of the record of Schmidt et al. (2006), whereas fragments counts and δ^{11}B-derived CO_2 at 871 are measured on the same samples. A cross-correlation function also shows no correlation between CO_2 offset and fragmentation (Figure S10).

While it seems unlikely the small offsets observed are fully explained by partial dissolution, the positive CO_2 offsets observed during some periods of high fragmentation index (Figure 5), are in line with trends observed in other species like *T. sacculifer* (sacc). For instance field studies observed lower δ^{11}B in *T. sacculifer* for core-top samples from deeper ocean sites bathed by waters with low calcite saturation state (Hönisch and Hemming, 2004, Seki et al., 2010). Tests of *T. sacculifer* can contain a significant proportion of gametogenic calcite (ranging 30 to 75% of the weight of pregametogenic calcite , Bé, 1980; Caron et al 1990) which forms at the end of the life cycle in deeper lower pH cold waters. It has been suggested that δ^{11}B is lower in gametogenic calcite than in the primary test (Ni et al., 2007) reflecting the digestion and expulsion of symbionts (Bé et al., 1983) before gametogenesis, driving a

586 relative acidification of the micro-environment (no CO_2 uptake by photosynthesis) around the
587 foraminifera (Zeebe et al. 2003; Hönisch et al,. 2003; Henehan et al. 2016), and movement to deeper
588 more acidic waters during that life-stage. It has been shown that this gametogenic calcite is more
589 resistant to dissolution (Hemleben et al., 1989; Wycech et al., 2018) resulting in partial dissolution
590 acting preferentially on ontogenic calcite, and driving δ^{11}B in the residual test to lower isotopic
591 composition.

592 However, while the decrease in δ^{11}B in tests of *T. sacculifer* found in corrosive waters is well explained
593 by the lighter isotopic composition of gametogenic calcite, *G. ruber* tests do not contain such
594 gametogenic calcite (Caron et al., 1990). Hence, if the observed occasional decrease in δ^{11}B (low pH,
595 high CO_2) was caused by partial dissolution, it needs to be explained by other processes. It should also
596 be considered that alternative measures and proxies of dissolution (e.g. benthic B/Ca as an indicator of
597 bottom water carbonate ion concentration) may yield more quantitative constraints on the importance
598 of dissolution in generating our observed CO_2 offsets. Some studies have shown that laboratory
599 dissolved specimens of *T. sacculifer* (Sadekov et al., 2010) and naturally dissolved specimens of *G.
600 ruber* (Iwasaki et al., 2019) undergo targeted partial preferential dissolution of the shell. However,
601 variations in intra-shell δ^{11}B are currently unknown due to limitations in laser ablation techniques that
602 currently impede a direct evaluation of δ^{11}B heterogeneity in foraminifera chambers. Future studies are
603 needed to constrain the δ^{11}B spatial distribution in foraminiferal shells caused by potential variations in
604 δ^{11}B from dissolution, ontogeny (e.g. Meilland et al., 2021) and/or vital effects (e.g. change in
605 photosymbiotic activity throughout the life cycle, Lombard et al., 2009, Henehan et al., 2013, Takagi
606 et al., 2019). In the absence of these constraints, we conclude that partial dissolution is unlikely to be a
607 significant driver of the δ^{11}B-CO_2 records we present here. Even though it was thought to be a species
608 susceptible to dissolution (Berger, 1970), we confirm that the δ^{11}B of *G. ruber* appears more resistant
609 to dissolution-driven modification than *T. sacculifer*.

610 *4.2.4.   Effect of dissolution on Mg/Ca and calculated CO_2.*

611 The direction of change of Mg/Ca with partial dissolution is towards lower ratios in partially dissolved
612 foraminifera (e.g. Brown and Elderfield, 1996; Dekens et al., 2002; Fehrenbacher and Martin, 2014). If
613 the Mg/Ca is impacted during periods of high fragmentation, the lower ratio would result in lower
614 temperatures leading to lower calculated CO_2 values (equation 7). This effect is opposite to the
615 occasional positive deviation of CO_2 observed during intervals of high fragmentation at ODP Site 999.
616 While the weak correlation between fragmentation and CO_2 precludes a firm interpretation of
617 dissolution effect, we conclude that the effect of partial dissolution on Mg/Ca ratio and resulting CO_2
618 (if any) are negligeable and not responsible for the CO_2 offsets observed during intervals of high
619 fragmentation.
620

621 *4.2.5.   Change in the second carbonate parameter, alkalinity.*

622 Past changes in TA are poorly constrained, although some constraints are starting to emerge for the late
623 Quaternary (e.g. Cartapanis et al., 2018). However, since pH is directly determined by δ^{11}B, pH defines
624 the ratio of alkalinity to DIC (see supplementary information S11). Hence, at any given pH, any change
625 in alkalinity must be counteracted by a change in DIC, which has the opposing effect on CO_2. This is
626 demonstrated by the tight relation between pH and CO_2 highlighted by our data (Figure 4). The largest
627 residual CO_2 is ~50 ppm at ODP 999. To produce an effective alkalinity-driven change in CO_2 of this
628 magnitude at a given pH requires an alkalinity reduction of about ~300 to 500 µmol/mol (supplementary
629 Figure S12). This is far larger than any expected change over a glacial cycle (Cartapanis et al., 2018,
630 Hönisch et al., 2009). We therefore rule out varying TA as the cause of the minor CO_2 offsets observed
631 (Figure 5).

632

    4.2.6   Improving the $\delta^{11}B$ -pH G. ruber calibration

634   A further potential cause for the minor offsets observed between $\delta^{11}B$-derived and ice core CO_2 could
635   be a small inaccuracy in the calibration between $\delta^{11}B$ of foraminifera and borate for *G. ruber* (Henehan
636   et al., 2013). Having the ice core data to compare with $\delta^{11}B$-derived CO_2 offers an opportunity to explore
637   the effect of altering the input variables of the pH-CO_2 calculation to see if doing so improves the fit to
638   ice-core values. Note that such an exercise is for illustrative purposes only because we seek to retain
639   the independence offered by the $\delta^{11}B$-calibrated data in the context of CO_2 forcing (section 4.3).
640   Nonetheless, in future work we suggest this calibration can be applied in tandem to the empirical
641   relationship of Henehan et al. (2013). The published (Henehan et al., 2013) and obtained optimised
642   calibration (Figure S13) are:

643    $$\delta^{11}B_{borate} = \frac{\delta^{11}B_{foram} - 8.87 (\pm 1.52)}{0.60 (\pm 0.09)} \quad \text{(Henehan et al., 2013)}$$

644

645    $$\delta^{11}B_{borate} = \frac{\delta^{11}B_{foram} - 6.49}{0.71} \quad \text{(optimised calibration)}$$

646

647   The newly calculated CO_2 with the updated calibration shows an improved average CO_2 offset (Figure
648   6) of -4 ± 36 (2σ) ppm (vs 13 ± 46 (2σ) ppm with the calibration of Henehan et al., 2013) and an RMSE
649   of 18 ppm (vs. 26 ppm with the published calibration).
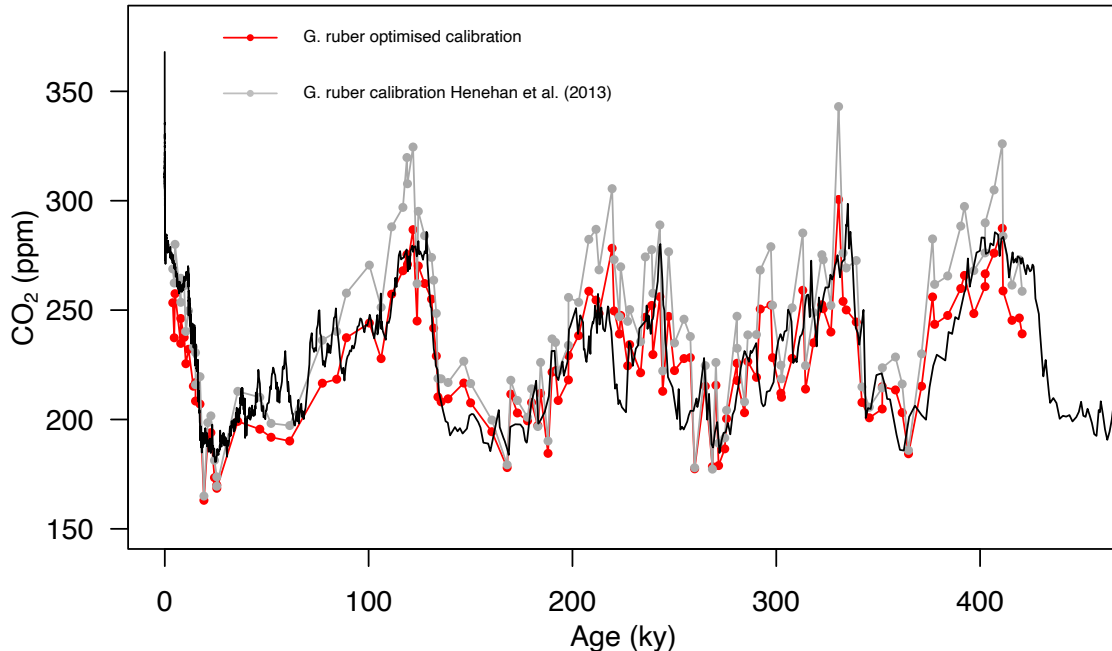
650

651   Figure 6. Composite $\delta^{11}B$-derived CO_2 from both core sites 999 and 871 using the published $\delta^{11}B_{borate-foram}$
652   calibration (grey points, Henehan et al., 2013) and the optimised calibration (red points). The black line is the
653   Antarctic composite ice core CO_2 record (Bereiter et al., 2015).

654   When analysing the CO_2 offset using the optimised *G. ruber* calibration and the fragmentation index
655   at each core location (same approach as Figure 5), we observe that intervals of high fragments

656 (defined as values above the upper quartile) are no longer preferentially associated with positive CO_2
657 offset (Figure S14). Intervals of high fragments occur 5% and 33% of the time, at Sites 999 and 871,
658 respectively, during positive CO_2 offsets (and 95 and 67% of the time during negative or no offset to
659 the ice cores).

660 This analysis shows that a small change in the borate *G. ruber* $\delta^{11}B$ calibration is enough to improve
661 the fit to the ice core and diminishes the apparent correlation between high fragmentation and
662 CO2 offset (Figure S14), and that uncertainty in the $\delta^{11}B_{foram-borate}$ calibration of Henehan et al. (2013)
663 can – at least partly – explain the minor discrepancies we observe between $\delta^{11}B$-derived and ice core
664 CO_2.

665 **4.3 Relative CO_2 forcing and pH.**

666 Our new pH data, added to the existing compilation, show a good agreement with the formalism
667 defined by Hain et al. (2018; Figure 4). It should be noted that CO_2 in this case is provided by the ice
668 core directly and is not estimated from the $\delta^{11}B$-derived pH. As discussed above, because these two
669 proxies are independent of one another, the slope of their relationship may be used to interrogate the
670 mechanisms of CO_2 change. Our data fall between the $CaCO_3$ (yellow plain line) and the DIC (dotted-
671 dashed blue line) endmembers suggesting that the CO_2 change observed on glacial-interglacial
672 timescales was driven by a mix of mechanisms rather than to a single cause. This is in line with
673 studies that require a number of mechanisms to explain glacial interglacials CO_2 change such as the
674 soft tissue pump, carbonate compensation pump, solubility pump (e.g. Brovkin et al., 2007, Kohfeld
675 and Ridgwell, 2009, Hain et al., 2010, Chalk et al., 2019, Sigman et al., 2021), and the disequilibrium
676 pump (Eggleston and Galbraith, 2018). We note that this is a preliminary interpretation because of
677 the sensitivity of our finding to pH uncertainty (section 3.4, Figure S7). To overcome this ambiguity
678 in estimating past ΔFCO_2 and to better deconvolve the driving mechanisms of glacial/interglacial CO_2
679 change, we recommend that future studies collect pH data at higher temporal resolution to examine
680 the change in slope through a glacial cycle and strive to further quantify and reduce uncertainties
681 related to pH determination.

682 The close agreement of the pH and ice core CO_2 data with the theoretical relationships has a number of
683 consequences for the reconstruction of CO_2 change during periods of Earth history beyond the ice core
684 CO_2 and climate records where constrains on $\delta^{11}B_{sw}$ and the second carbonate parameter and
685 temperature are uncertain. The ΔpH formalism still requires an estimation of $\delta^{11}B_{sw}$ and temperature
686 (for the pK_B term, equation 5) however, as discussed in Hain et al. (2018), while absolute reconstruction
687 of pH is significantly influenced by estimates of $\delta^{11}B_{sw}$ and temperature, reconstruction of relative pH
688 change (ΔpH) is inherently much less sensitive to these input variables.

689 Reconstructing ΔF_{CO2} from ΔpH is ideally applicable only on relatively short timescales less than 1
690 Myrs, when $\delta^{11}B_{sw}$ is likely to be invariant given the multi-million year residence time of boron in the
691 ocean (Lemarchand et al., 2002, Greenop et al., 2017). Furthermore, to reconstruct ΔF_{CO2} (and thus
692 climate sensitivity to CO_2), the formalism can be applied as long as, in equation 2, ΔpH remains the
693 overwhelming control. This is dependent on the residence time of carbon in the ocean with respect to
694 silicate weathering – approximately one million years (Hain et al., 2018) such that net carbon addition
695 to or removal from the Earth System through volcanic outgassing or silicate weathering is likely to be
696 minor over the million-year timescale. However, during some short events, such as for instance the
697 Palaeocene-Eocene Thermal Maximum, considerable carbon was added to the system in <200 kyr (e.g.
698 Gutjahr et al., 2017) invalidating the formulation described in equation 2 on these intervals. We also
699 emphasize that this formalism is only valid as long as core sites remain in equilibrium with the
700 atmosphere.

701

4.4 Caveats and future studies.

The aim of this study is to evaluate the capacity of the δ^{11}B-pH proxy in *G. ruber* to accurately reconstruct atmospheric CO_2 in the past. The overall agreement with the high confidence ice core CO_2 (e.g. Bereiter et al., 2015) is very promising and gives confidence to δ^{11}B-derived CO_2 reconstructions beyond the ice core record (>800 ky). We have however identified occasional, minor offsets between the two records and explored potential drivers (partial dissolution, δ^{11}B borate-foram calibration, local air-sea disequilibrium). It is likely that the minor disagreement observed (Figure 5) has a combination of drivers and that a single mechanism is not solely responsible for the CO_2 offsets observed. To confirm these trends, we recommend future work to focus on the following:

(1) The improved δ^{11}B calibration approach should be tested at more core locations. We note that the improved calibration to the ice core records reported here was achieved using data from two sites. While care is taken in the choice of study site to minimize air-sea CO_2 disequilibrium and sediment dissolution, the newly defined improved $\delta^{11}B_{borate-foram}$ calibration should be seen as an exercise that is tailored to the available data in this study, and future high-resolution studies can apply the method used here (section 4.2.6) to further test how the *G. ruber* calibration changes if CO_2 offsets occur in a similar fashion (i.e at a particular time in each glacial cycles). We note the importance of high resolution (at least 3 ky) sampling in future studies because most CO_2 offsets observed are short lived.

(2) A multiproxy approach is ideally needed. In particular, reliable indicators of temperature and productivity, to assess change in upwelling and foraminifera ecology. We encourage future studies to expand high resolution boron-derived CO_2 record and ancillary data (C and O isotopes, proxy of carbonate preservation and bottom water corrosiveness, biological productivity) to further constrain the capacity of the boron isotope pH/CO_2 proxy to generate reliable CO_2 records. As more recent IODP expeditions include porewater data, constraints on bottom water conditions and degree of corrosiveness at a given site will become available to evaluate the impact on δ^{11}B signals in foraminifera.

(3) Efforts should continue to decrease the analytical uncertainty associated with a δ^{11}B measurement by MC-ICPMS because this still accounts for ~40% of the total uncertainty associated with each δ^{11}B-derived CO_2 estimate.

(4) We find little evidence to suggest that partial dissolution of foraminiferal tests (*G. ruber*) is a major driver of uncertainty in δ^{11}B–derived CO_2 estimates but well constrained dissolution experiments are desirable because of site-to-site differences in foraminifera taphonomy.

5. Conclusion.

We carried out the most thorough test to date of the δ^{11}B–pH (CO_2) proxy by comparing new high-resolution (3 to 6 ky per sample) boron isotope–based pH and CO_2 at two locations with CO_2 from the ice core record. Results suggest that the boron isotope proxy is robust and suited to reconstructing CO_2 to a precision of ±46 ppm (2σ, RMSE =26 ppm) over this interval, with little or no systematic bias shown by a mean residual of 13±46 (2σ) ppm . This provides high confidence to the application of the proxy beyond the reach of the ice core records.

Despite the overall good agreement, there are some minor short-lived CO_2 offsets that appear to have some temporal structure and we explored a number of possible drivers. A visual correlation between CO_2 offset and fragmentation index at core site 999 is observed (Figure 5) but is not statistically significant. The effect of partial dissolution on δ^{11}B in *G. ruber* appears to be negligeable in our record, but the possible heterogeneity of δ^{11}B within shells as well as variable susceptibly to dissolution of the different parts of the foraminifera, encourage further exploration.

746 A revised $\delta^{11}B$ borate–foram calibration was calculated by minimising the offset between $\delta^{11}B$−derived
747 CO_2 and ice core CO_2 using published calibration (Henehan et al., 2013). While the new calibration
748 improves the fit to the ice core records, we caution against its use to estimate CO_2 given that it is no
749 longer independent of the ice core or the assumptions we make here to calculate CO_2 (i.e. that TA is
750 constant).

751 The formalism established by Hain et al. (2018) is robust, showing that relative CO_2 forcing in the past
752 can be determined from pH change alone, even in the face of significant uncertainty in $\delta^{11}B$ of seawater
753 and without the need to determine a second carbonate parameter. This will not only be of great interest
754 to determine CO_2 forcing in ancient geological times where $\delta^{11}B$ of seawater and a second carbonate
755 parameter are poorly constrained, but the nature of the observed relationship over the last 400 kyr
756 confirms that multiple drivers are likely responsible for glacial-interglacial CO_2 change.

6. Data availability.

All raw data are provided as supplementary information.

7. Author contribution.

E.d.l.V generated boron isotope and elemental data and wrote the manuscript. E.d.l.V, T.B.C, M.P.H
and G.L.F analysed the data. G.L.F, T.B.C, M.P.H and P.A.W contributed to the editing and
reviewing of the manuscript. M.W, R.G and D.C generated oxygen and carbon isotope data and
fragmentation index data. R.G and D.C were supervised by T.B.C and G.L.F. C.L assisted with
foraminifera picking and boron isotope analysis. E.d.l.V, T.B.C and G.L.F designed the research.

8. Competing interest.

The authors declare they have no conflict of interest.

9. Acknowledgment.

We warmly thank J. Andy Milton for assistance in MC-ICPMS and ICPMS analysis, and members of
the "B-team", Agnes Michalik and Matthew Cooper for clean laboratory assistance. We thank
William Gray and one anonymous reviewer for insightful comments that improved the manuscript.
This work was funded by NERC grant NE/P011381/1 to GLF, PAW, TBC and MPH and by Royal
Society Wolfson Awards to both GLF and PAW.

10. References.

Ahn, J., et al. (2012). "Atmospheric CO2 over the last 1000 years: A high-resolution record
from the West Antarctic Ice Sheet (WAIS) Divide ice core." Global Biogeochemical Cycles
26(2).

Anagnostou, E., et al. (2020). "Proxy evidence for state-dependence of climate sensitivity in
the Eocene greenhouse." Nature communications **11**(1): 1-9.

Anagnostou, E., et al. (2016). "Changing atmospheric CO2 concentration was the primary
driver of early Cenozoic climate." Nature **533**(7603): 380-384.

Anagnostou, E., et al. (2019). "Calibration of the pH-δ11B and temperature-Mg/Li proxies in
the long-lived high-latitude crustose coralline red alga Clathromorphum compactum via
controlled laboratory experiments." Geochimica et Cosmochimica Acta **254**: 142-155.

Anand, P., et al. (2003). "Calibration of Mg/Ca thermometry in planktonic foraminifera from
a sediment trap time series." Paleoceanography **18**(2).

Anderson, R. F., et al. (2019). "Deep-sea oxygen depletion and ocean carbon sequestration during the last ice age." Global Biogeochemical Cycles **33**(3): 301-317.

Aurahs, R., et al. (2011). "A revised taxonomic and phylogenetic concept for the planktonic foraminifer species Globigerinoides ruber based on molecular and morphometric evidence." Marine Micropaleontology **79**(1-2): 1-14.

Barker, S., et al. (2006). "Globally increased pelagic carbonate production during the Mid-Brunhes dissolution interval and the CO2 paradox of MIS 11." Quaternary Science Reviews **25**(23-24): 3278-3293.

Barker, S., et al. (2003). "A study of cleaning procedures used for foraminiferal Mg/Ca paleothermometry." Geochemistry, Geophysics, Geosystems **4**(9).

Bé, A. (1980). "Gametogenic calcification in a spinose planktonic foraminifer, Globigerinoides sacculifer (Brady)." Marine Micropaleontology **5**: 283-310.

Bé, A. W., et al. (1983). "Sequence of morphological and cytoplasmic changes during gametogenesis in the planktonic foraminifer Globigerinoides sacculifer (Brady)." Micropaleontology: 310-325.

Bereiter, B., et al. (2015). "Revision of the EPICA Dome C CO2 record from 800 to 600 kyr before present." Geophysical Research Letters **42**(2): 542-549.

Berger, W. H. (1970). "Planktonic foraminifera: selective solution and the lysocline." Marine Geology **8**(2): 111-138.

Boyle, E. A. (1988). "The role of vertical chemical fractionation in controlling late Quaternary atmospheric carbon dioxide." Journal of Geophysical Research: Oceans **93**(C12): 15701-15714.

Boyle, E. A. (1988). "Vertical oceanic nutrient fractionation and glacial/interglacial CO2cycles." Nature **331**(6151): 55-56.

Brovkin, V., et al. (2007). "Lowering of glacial atmospheric CO2 in response to changes in oceanic circulation and marine biogeochemistry." Paleoceanography **22**(4).

Brown, S. J. and H. Elderfield (1996). "Variations in Mg/Ca and Sr/Ca ratios of planktonic foraminifera caused by postdepositional dissolution: Evidence of shallow Mg-dependent dissolution." Paleoceanography **11**(5): 543-551.

Caron, D. A., et al. (1990). "Effects of gametogenesis on test structure and dissolution of some spinose planktonic foraminifera and implications for test preservation." Marine Micropaleontology **16**(1-2): 93-116.

Cartapanis, O., et al. (2018). "Carbon burial in deep-sea sediment and implications for oceanic inventories of carbon and alkalinity over the last glacial cycle." Climate of the Past **14**(11): 1819-1850.

846 Carter, A., et al. (2017). "Differing oxygen isotopic signals of two Globigerinoides ruber
847 (white) morphotypes in the East China Sea: Implications for paleoenvironmental
848 reconstructions." Marine Micropaleontology **131**: 1-9.
849

850 Chalk, T., et al. (2019). "Dynamic storage of glacial CO_2 in the Atlantic Ocean revealed by
851 boron [CO_3^{2-}] and pH records." Earth and Planetary Science Letters **510**: 1-11.
852

853 Chalk, T. B., et al. (2017). "Causes of ice age intensification across the Mid-Pleistocene
854 Transition." Proceedings of the National Academy of Sciences **114**(50): 13114-13119.
855

856 de Garidel-Thoron, T., et al. (2005). "Stable sea surface temperatures in the western Pacific
857 warm pool over the past 1.75 million years." Nature **433**(7023): 294-298.
858

859 De La Vega, E., et al. (2020). "Atmospheric CO_2 during the Mid-Piacenzian Warm Period and
860 the M2 glaciation." Scientific reports **10**(1): 1-8.
861

862 Dekens, P. S., et al. (2002). "Core top calibration of Mg/Ca in tropical foraminifera: Refining
863 paleotemperature estimation." Geochemistry, Geophysics, Geosystems **3**(4): 1-29.
864

865 Dyez, K. A., et al. (2018). "Early Pleistocene obliquity-scale pCO_2 variability at~ 1.5 million
866 years ago." Paleoceanography and Paleoclimatology **33**(11): 1270-1291.
867

868 Dyez, K. A. and A. C. Ravelo (2013). "Late Pleistocene tropical Pacific temperature sensitivity
869 to radiative greenhouse gas forcing." Geology **41**(1): 23-26.
870

871 Dyez, K. A. and A. C. Ravelo (2014). "Dynamical changes in the tropical Pacific warm pool
872 and zonal SST gradient during the Pleistocene." Geophysical Research Letters **41**(21): 7626-
873 7633.
874

875 Eggleston, S. and E. D. Galbraith (2018). "The devil's in the disequilibrium: multi-component
876 analysis of dissolved carbon and oxygen changes under a broad range of forcings in a general
877 circulation model." Biogeosciences **15**(12): 3761-3777.
878

879

880 Farrell, J. W. and W. L. Prell (1989). "Climatic change and $CaCO_3$ preservation: An 800,000
881 year bathymetric reconstruction from the central equatorial Pacific Ocean." Paleoceanography
882 **4**(4): 447-466.
883

884 Fehrenbacher, J. S. and P. A. Martin (2014). "Exploring the dissolution effect on the intrashell
885 Mg/Ca variability of the planktic foraminifer Globigerinoides ruber." Paleoceanography **29**(9):
886 854-868.
887

888 Foster, G. (2008). "Seawater pH, pCO_2 and [CO_3^{2-}] variations in the Caribbean Sea over the
889 last 130 kyr: A boron isotope and B/Ca study of planktic foraminifera." Earth and Planetary
890 Science Letters **271**(1-4): 254-266.
891

892 Foster, G., et al. (2010). "Boron and magnesium isotopic composition of seawater."
893 Geochemistry, Geophysics, Geosystems **11**(8).
894

895 Foster, G. L., et al. (2012). "The evolution of pCO2, ice volume and climate during the middle
896 Miocene." Earth and Planetary Science Letters **341**: 243-254.
897

898 Foster, G. L., et al. (2013). "Interlaboratory comparison of boron isotope analyses of boric acid,
899 seawater and marine CaCO3 by MC-ICPMS and NTIMS." Chemical Geology **358**: 1-14.
900

901

902 Foster, G. L. and J. W. Rae (2016). "Reconstructing ocean pH with boron isotopes in
903 foraminifera." Annual Review of Earth and Planetary Sciences **44**: 207-237.
904

905 Gray, W. R. and D. Evans (2019). "Nonthermal influences on Mg/Ca in planktonic
906 foraminifera: A review of culture studies and application to the last glacial maximum."
907 Paleoceanography and Paleoclimatology **34**(3): 306-315.
908

909 Gray, W. R., et al. (2018). "The effects of temperature, salinity, and the carbonate system on
910 Mg/Ca in Globigerinoides ruber (white): A global sediment trap calibration." Earth and
911 Planetary Science Letters **482**: 607-620.
912

913

914 Greenop, R., et al. (2017). "A record of Neogene seawater $\delta11B$ reconstructed from paired
915 $\delta11B$ analyses on benthic and planktic foraminifera." Climate of the Past **13**(2): 149-170.
916

917 Guillermic, M., et al. (2022). "Atmospheric CO 2 estimates for the Miocene to Pleistocene
918 based on foraminiferal δ 11 B at Ocean Drilling Program Sites 806 and 807 in the Western
919 Equatorial Pacific." Climate of the Past **18**(2): 183-207.
920

921 Gutjahr, M., et al. (2017). "Very large release of mostly volcanic carbon during the Palaeocene–
922 Eocene Thermal Maximum." Nature **548**(7669): 573-577.
923

924 Hain, M., et al. (2018). "Robust constraints on past CO2 climate forcing from the boron isotope
925 proxy." Paleoceanography and Paleoclimatology **33**(10): 1099-1115.
926

927 Hain, M. P., et al. (2014). "8.18–The biological Pump in the Past." Reference Module in Earth
928 Systems and Environmental Sciences, Treatise on Geochemistry (Second Edition), The Oceans
929 and Marine Geochemistry **8**: 485-517.
930

931

932 Hain, M. P., et al. (2010). "Carbon dioxide effects of Antarctic stratification, North Atlantic
933 Intermediate Water formation, and subantarctic nutrient drawdown during the last ice age:
934 Diagnosis and synthesis in a geochemical box model." Global Biogeochemical Cycles **24**(4).
935

936 Hansen, J., et al. (2008). "Target atmospheric CO2: Where should humanity aim?" arXiv
937 preprint arXiv:0804.1126.
938

939 Harper, D., et al. (2020). "The magnitude of surface ocean acidification and carbon release
940 during Eocene Thermal Maximum 2 (ETM-2) and the Paleocene-Eocene Thermal Maximum
941 (PETM)." Paleoceanography and Paleoclimatology **35**(2): e2019PA003699.
942

943 Hemleben, C., et al. (1989). Modern Planktonic Foraminifera, Springer-Verlag.
944

945 Henehan, M. J., et al. (2016). "A new boron isotope-pH calibration for Orbulina universa, with
946 implications for understanding and accounting for 'vital effects'." Earth and Planetary Science
947 Letters **454**: 282-292.

949 Henehan, M. J., et al. (2015). "Evaluating the utility of B/C a ratios in planktic foraminifera as
950 a proxy for the carbonate system: A case study of G lobigerinoides ruber." Geochemistry,
951 Geophysics, Geosystems **16**(4): 1052-1069.

953 Henehan, M. J., et al. (2013). "Calibration of the boron isotope proxy in the planktonic
954 foraminifera Globigerinoides ruber for use in palaeo-CO2 reconstruction." Earth and Planetary
955 Science Letters **364**: 111-122.

957 Henehan, M. J., et al. (2019). "Rapid ocean acidification and protracted Earth system recovery
958 followed the end-Cretaceous Chicxulub impact." Proceedings of the National Academy of
959 Sciences **116**(45): 22500-22504.

961 Hönisch, B., et al. (2003). "The influence of symbiont photosynthesis on the boron isotopic
962 composition of foraminifera shells." Marine Micropaleontology **49**(1-2): 87-96.

964 Hönisch, B. and N. G. Hemming (2004). "Ground-truthing the boron isotope-paleo-pH proxy
965 in planktonic foraminifera shells: Partial dissolution and shell size effects." Paleoceanography
966 **19**(4).

968 Hönisch, B. and N. G. Hemming (2005). "Surface ocean pH response to variations in pCO2
969 through two full glacial cycles." Earth and Planetary Science Letters **236**(1-2): 305-314.

971 Hönisch, B., et al. (2009). "Atmospheric carbon dioxide concentration across the mid-
972 Pleistocene transition." Science **324**(5934): 1551-1554.

974 Howard, W. R. and W. L. Prell (1994). "Late Quaternary CaCO3 production and preservation
975 in the Southern Ocean: Implications for oceanic and atmospheric carbon cycling."
976 Paleoceanography **9**(3): 453-482.

978 Iwasaki, S., et al. (2019). "Micro-CT Scanning of Tests of Three Planktic Foraminiferal Species
979 to Clarify DissolutionProcess and Progress." Geochemistry, Geophysics, Geosystems **20**(12):
980 6051-6065.

982 John, S. G. and J. F. Adkins (2010). "Analysis of dissolved iron isotopes in seawater." Marine
983 chemistry **119**(1-4): 65-76.

985 Johns, W. E., et al. (2002). "On the Atlantic inflow to the Caribbean Sea." Deep sea research
986 part I: Oceanographic research papers **49**(2): 211-243.

988 Klochko, K., et al. (2006). "Experimental measurement of boron isotope fractionation in
989 seawater." Earth and Planetary Science Letters **248**(1-2): 276-285.

991 Kohfeld, K. E. and A. Ridgwell (2009). "Glacial-interglacial variability in atmospheric CO2."
992 Surface ocean-lower atmosphere processes **187**: 251-286.

994 Lauvset, S. K., et al. (2022). "GLODAPv2. 2022: the latest version of the global interior ocean
995 biogeochemical data product." Earth System Science Data Discussions **2022**: 1-37.
996
997
998 Lee, K., et al. (2010). "The universal ratio of boron to chlorinity for the North Pacific and North
999 Atlantic oceans." Geochimica et Cosmochimica Acta **74**(6): 1801-1811.
1000
1001 Lemarchand, D., et al. (2002). "Boron isotope systematics in large rivers: implications for the
1002 marine boron budget and paleo-pH reconstruction over the Cenozoic." Chemical Geology
1003 **190**(1-4): 123-140.
1004
1005 Lisiecki, L. E. and M. E. Raymo (2005). "A Plio-Pleistocene stack of 57 globally distributed
1006 benthic δ 18 O records." Paleoceanography **20**: 1-17.
1007
1008 Lombard1, F., et al. (2009). "Temperature effect on respiration and photosynthesis of the
1009 symbiont-bearing planktonic foraminifera Globigerinoides ruber, Orbulina universa, and
1010 Globigerinella siphonifera." Limnology and Oceanography **54**(1): 210-218.
1011
1012 Lueker, T. J., et al. (2000). "Ocean pCO2 calculated from dissolved inorganic carbon,
1013 alkalinity, and equations for K1 and K2: validation based on laboratory measurements of CO2
1014 in gas and seawater at equilibrium." Marine chemistry **70**(1-3): 105-119.
1015
1016 Lüthi, D., et al. (2008). "High-resolution carbon dioxide concentration record 650,000–800,000
1017 years before present." Nature **453**(7193): 379-382.
1018
1019 Marchitto, T., et al. (2014). "Improved oxygen isotope temperature calibrations for
1020 cosmopolitan benthic foraminifera." Geochimica et Cosmochimica Acta **130**: 1-11.
1021
1022 Martínez-Botí, M., et al. (2015). "Plio-Pleistocene climate sensitivity evaluated using high-
1023 resolution CO 2 records." Nature **518**(7537): 49.
1024
1025 Meilland, J., et al. (2021). "Population dynamics and reproduction strategies of planktonic
1026 foraminifera in the open ocean." Biogeosciences **18**(20): 5789-5809.
1027
1028 Ni, Y., et al. (2007). "A core top assessment of proxies for the ocean carbonate system in
1029 surface-dwelling foraminifers." Paleoceanography **22**(3).
1030
1031 Numberger, L., et al. (2009). "Habitats, abundance patterns and isotopic signals of
1032 morphotypes of the planktonic foraminifer Globigerinoides ruber (d'Orbigny) in the eastern
1033 Mediterranean Sea since the Marine Isotopic Stage 12." Marine Micropaleontology **73**(1-2):
1034 90-104.
1035
1036 Olsen, A., et al. (2016). "The Global Ocean Data Analysis Project version 2 (GLODAPv2)–an
1037 internally consistent data product for the world ocean." Earth System Science Data **8**(2): 297-
1038 323.
1039
1040 Olsen, A., et al. (2004). "Sea–air flux of CO2 in the Caribbean Sea estimated using in situ and
1041 remote sensing data." Remote Sensing of Environment **89**(3): 309-325.
1042

Oppo, D. and S. Lehman (1993). "Mid-depth circulation of the subpolar North Atlantic during the last glacial maximum." Science 259(5098): 1148-1152.

Paillard, D., et al. (1996). "Macintosh program performs time-series analysis." Eos, Transactions American Geophysical Union 77(39): 379-379.

Penman, D. E., et al. (2014). "Rapid and sustained surface ocean acidification during the Paleocene-Eocene Thermal Maximum." Paleoceanography 29(5): 357-369.

Petit, J.-R., et al. (1999). "Climate and atmospheric history of the past 420,000 years from the Vostok ice core, Antarctica." Nature 399(6735): 429-436.

Premoli-Silva, I. (1993). Shipboard Scientific Party, 1993a Site 871. Proc. ODP, Init. Repts.

Rae, J. W., et al. (2011). "Boron isotopes and B/Ca in benthic foraminifera: Proxies for the deep ocean carbonate system." Earth and Planetary Science Letters 302(3-4): 403-413.

Raitzsch, M., et al. (2018). "Boron isotope-based seasonal paleo-pH reconstruction for the Southeast Atlantic–A multispecies approach using habitat preference of planktonic foraminifera." Earth and Planetary Science Letters 487: 138-150.

Rebotim, A., et al. (2017). "Factors controlling the depth habitat of planktonic foraminifera in the subtropical eastern North Atlantic." Biogeosciences 14(4): 827-859.

Rohling, E., et al. (2013). "Making sense of palaeoclimate sensitivity (vol 491, pg 683, 2012)." Nature 494(7435): 130-130.

Rohling, E. J., et al. (2018). "Comparing climate sensitivity, past and present." Annual Review of Marine Science 10: 261-288.

Sadekov, A. Y., et al. (2010). "Effects of seafloor and laboratory dissolution on the Mg/Ca composition of Globigerinoides sacculifer and Orbulina universa tests—A laser ablation ICPMS microanalysis perspective." Earth and Planetary Science Letters 292(3-4): 312-324.

Sanyal, A., et al. (1995). "Evidence for a higher pH in the glacial ocean from boron isotopes in foraminifera." Nature 373(6511): 234-236.

Schlitzer, R. (2022). "Ocean data view."

Schmidt, M. W., et al. (2006). "Western Caribbean sea surface temperatures during the late Quaternary." Geochemistry, Geophysics, Geosystems 7(2).

Seki, O., et al. (2010). "Alkenone and boron-based Pliocene pCO2 records." Earth and Planetary Science Letters 292(1-2): 201-211.

Sexton, P. F. and S. Barker (2012). "Onset of 'Pacific-style' deep-sea sedimentary carbonate cycles at the mid-Pleistocene transition." Earth and Planetary Science Letters 321: 81-94.

Siegenthaler, U., et al. (2005). "Stable carbon cycle climate relationship during the Late Pleistocene." Science **310**(5752): 1313-1317.

Sigman, D. M., et al. (2021). "The Southern Ocean during the ice ages: A review of the Antarctic surface isolation hypothesis, with comparison to the North Pacific." Quaternary Science Reviews **254**: 106732.

Sigman, D. M., et al. (2010). "The polar ocean and glacial cycles in atmospheric CO 2 concentration." Nature **466**(7302): 47-55.

Sigman, D. M., et al. (1998). "The calcite lysocline as a constraint on glacial/interglacial low-latitude production changes." Global Biogeochemical Cycles **12**(3): 409-427.

Spero, H. J., et al. (1997). "Effect of seawater carbonate concentration on foraminiferal carbon and oxygen isotopes." Nature **390**(6659): 497-500.

Steinke, S., et al. (2005). "Mg/Ca ratios of two Globigerinoides ruber (white) morphotypes: Implications for reconstructing past tropical/subtropical surface water conditions." Geochemistry, Geophysics, Geosystems **6**(11).

Takagi, H., et al. (2019). "Characterizing photosymbiosis in modern planktonic foraminifera." Biogeosciences **16**(17): 3377-3396.

Takahashi, T., et al. (2009). "Climatological mean and decadal change in surface ocean pCO2, and net sea–air CO2 flux over the global oceans." Deep Sea Research Part II: Topical Studies in Oceanography **56**(8-10): 554-577.

Toggweiler, J. (1999). "Variation of atmospheric CO2 by ventilation of the ocean's deepest water." Paleoceanography **14**(5): 571-588.

Wang, L. (2000). "Isotopic signals in two morphotypes of Globigerinoides ruber (white) from the South China Sea: implications for monsoon climate change during the last glacial cycle." Palaeogeography, Palaeoclimatology, Palaeoecology **161**(3-4): 381-394.

Wycech, J. B., et al. (2018). "Combined effects of gametogenic calcification and dissolution on δ18O measurements of the planktic foraminifer Trilobatus sacculifer." Geochemistry, Geophysics, Geosystems **19**(11): 4487-4501.

York, D., et al. (2004). "Unified equations for the slope, intercept, and standard errors of the best straight line." American journal of physics **72**(3): 367-375.

Zeebe, R. E. and D. Wolf-Gladrow (2001). CO2 in seawater: equilibrium, kinetics, isotopes, Gulf Professional Publishing.

Zeebe, R. E., et al. (2003). "Vital effects in foraminifera do not compromise the use of δ11B as a paleo-pH indicator: Evidence from modeling." Paleoceanography **18**(2).